The influence of roadsurface on powerloss

The design of a experimental apparatus that mimics roadsurfaces and measures powerloss

Master thesis

Quinten Bongers

Delft University of Technology

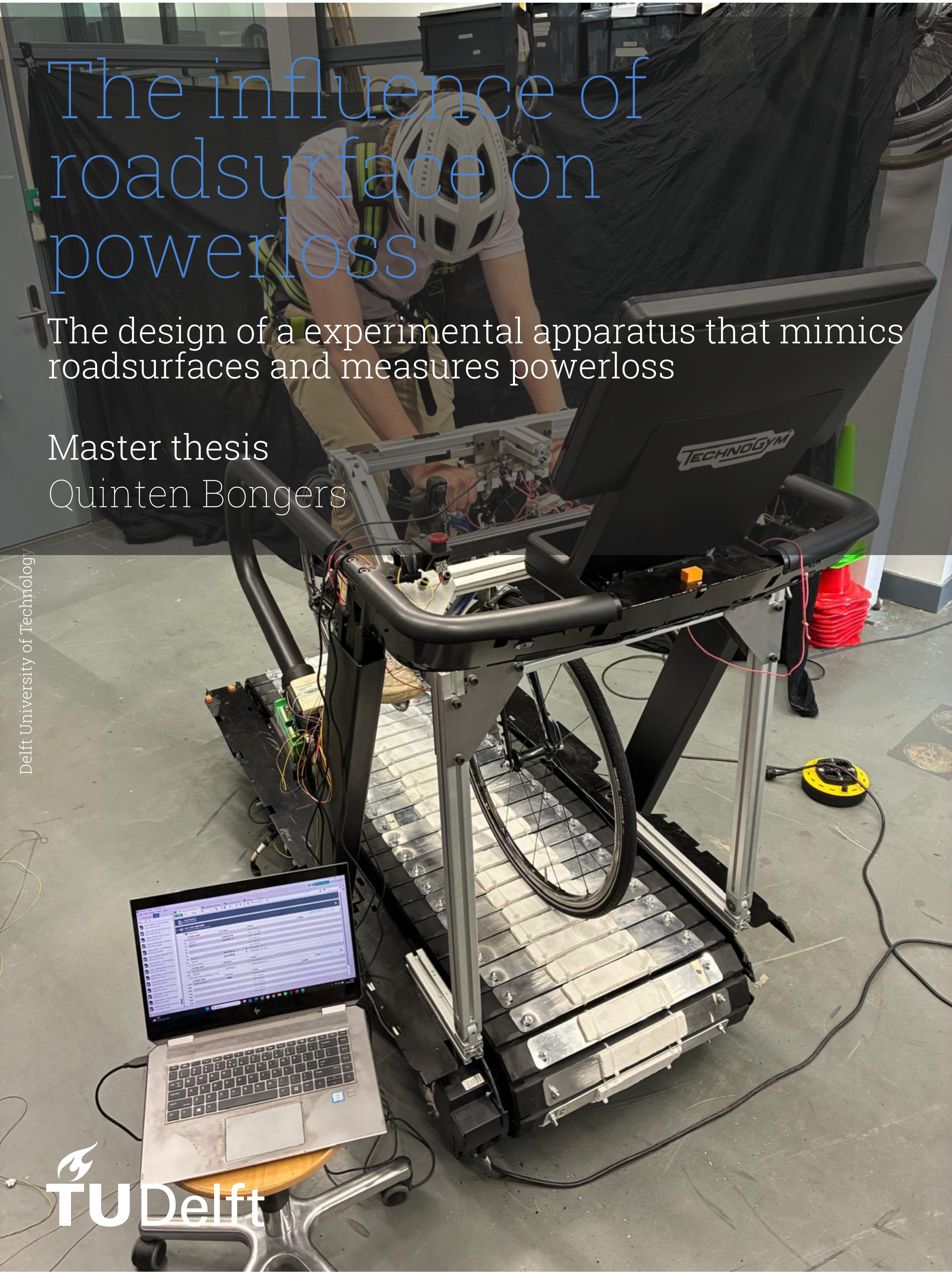

The influence of roadsurface on powerloss

The design of a experimental apparatus that mimics roadsurfaces and measures powerloss

by

Quinten Bongers

Quinten Bongers

5141303

Daily supervisor: Dr. J.K. Moore
Secondary supervisor: Dr. G. Papaiaonnou
Committee member: Prof. dr. Ir. R. Happee
Faculty: Faculty of Mechanical Engineering, Delft

Preface

A massive thank you to Jason Moore and Georgios Papaioannou for guiding me during my master thesis. The feedback and discussions during our weekly meetings were of great value and helped a lot in getting to this result. I hope this thesis will provide a platform for future research.

Thanks to the bikelab for being a great workplace to design, build, and test this machine. Additionally, thank you to all the members of the bikelab for providing support and advice throughout this thesis; your input has been of great value.

A massive thank you also goes to my family for supporting me during my studies in Delft. Once in a while, some parental advice was genuinely useful in figuring out what the next step should be.

This thesis was quite challenging at certain times, but two people were especially helpful along the way. Special mention to Thijn Hoekstra and Eva van der Dijs for their support throughout my thesis: being a sparring partner, doing design reviews, and asking the right questions whenever I got stuck.

There are two more things I have not thanked yet, but both were a crucial part of my time in Delft. The first is my laptop, which endured thousands of hours of simulations, FEM analyses, and coding, and always performed flawlessly. The second is the coffee machines at the TU Delft campus and at home. Over the course of this thesis, an estimated 1200 coffees were consumed. Over my entire time in Delft, that number is closer to 7,000, but it was always nice to have a ”KOFF?”.

This master thesis also marks the end of my time in Delft. I still remember my first lecture in statics in the Aula; time flies when you are having fun... The most fun I had was during my time at Forze Hydrogen Racing: memories and experiences I will never forget, and, most importantly, friends I will never forget either.

Thank you, Delft!

Quinten Bongers - July 2026

Statement on Use of AI

During the preparation of this work, the author used Claude Opus-4.6 as a tool to assist with coding, grammar correction and written expression. All content written with its support was reviewed and edited by the author, who takes full responsibility for the final version of the text and content of the publication.

Abstract

Road-induced vibrations dissipate energy through the bicycle structure and rider's body beyond what classical rolling resistance predicts. To measure this effect a laboratory apparatus is used that reproduces realistic road surface characteristics. This thesis presents the design, construction, and validation of such an apparatus and characterises the powerloss on a 3D-printed klinker road surface across six speeds (5–30 km/h) and five tire pressures (3.5–5.5 bar).

The setup measures the total resistive force acting on an athlete and racing bicycle using two loadcells: a main loadcell and an interface loadcell that captures the longitudinal force exerted by a two-bar linkage stabilization mechanism, isolated from the vertical load by a parallelogram flexure. Multiplying this force by the belt speed gives the powerloss. The force is measured with an expanded uncertainty of $\pm 0.41\ N$ at the 95% confidence level, corresponding to a powerloss uncertainty of at most 3.4 W at 30 km/h.

Powerloss increases approximately linearly with speed for all pressures, ranging from about 30 W at 5 km/h to 234 W at 30 km/h. Much of this loss is not classical rolling resistance: at 30 km/h the classical term accounts for only about 82 W, so roughly 64% of the total powerloss is attributed to vibrational losses. Tire pressure has a smaller effect: depending on the speed setpoint, an optimal tire pressure can be identified, although at lower speeds the error bars overlap and no clear optimum can be determined. The near-linear speed dependence shows that although the vibrational losses are large, their speed-growing quadratic component remains weak on the relatively smooth klinker surface (BRI ≈ 40). A stiffer underlayer and a rougher surface are recommended before the apparatus can be used to quantify vibration transmission from the road surface through the bicycle to the rider's body.

Contents

1 Introduction

1.1. Motivation

Over the past decade, professional cyclists have increasingly shifted towards wider tyres at lower pressures, driven by the recognition that road surface characteristics influence power loss beyond what classical rolling resistance alone predicts. In stage races such as the Tour de France, teams continuously optimise tyre choice and inflation pressure to minimise resistive losses on varying road surfaces. This trend becomes most pronounced at races such as Paris–Roubaix, where competitors traverse more than 50 km of cobblestone sectors, known locally as *pavé*, at race speeds exceeding 40 km/h.

Cycling is one of the most energy-efficient modes of transport, yet a significant portion of a cyclist's effort is lost to resistive forces at the tyre–road interface. Classical rolling resistance describes the force arising from viscoelastic deformation of the tyre at the contact patch and is expressed as $F_{\mathrm{rr}} = C_{\mathrm{rr}} \cdot F_N$, where C_{rr} is the rolling resistance coefficient and F_N is the normal force at the contact patch [1], [2]. On smooth surfaces this term dominates tyre-related losses and is approximately independent of speed [2]. On rough surfaces, however, road irregularities continuously excite oscillations in the tyre–bicycle–rider system, dissipating additional energy through the bicycle structure and the rider's body through a mechanism that cannot be captured by C_{rr} alone. This additional dissipation is referred to here as vibrational power loss.

The magnitude of vibrational power loss is governed by the frequency response function (FRF) of the bicycle–rider system. Louhghalam et al. [3] formalised this for vehicle–road interaction, showing analytically that vibrational power loss scales quadratically with the FRF of the vehicle system. Because bicycles lack dedicated suspension and the rider's body is directly coupled to the frame through the saddle, handlebars and pedals, the FRF of the bicycle–rider system differs fundamentally from that of a car: it is nonlinear and highly rider-dependent [4], [5]. Lépine et al. [6] demonstrated experimentally that changes in rider posture and hand position alone alter vibration transmissibility at the handlebar and seatpost by several $\mathrm{m/s^2}$, meaning that two riders on identical equipment can experience substantially different vibrational power losses on the same surface. Wilson and Schmidt [7] further showed that the power absorbed by the rider scales with vibration amplitude squared and is especially sensitive to excitation frequencies in the range of 9–50 Hz, confirming that surface roughness can have a disproportionately large effect on total power loss. Beyond competitive performance, prolonged exposure to road-induced vibrations is associated with musculoskeletal fatigue and discomfort Lépine et al. [6], and similar concerns extend to other vehicle types such as cargo bikes and strollers, where vibration exposure affects vulnerable passengers Dell'Orto et al. [8].

Since vibrational power loss manifests as an increase in the total rolling resistance force, measuring it requires accurate experimental methods for quantifying rolling resistance. A variety of such approaches have been developed in the literature. Indirect methods estimate rolling losses from other measurable quantities:

- The Chung method uses a power meter and virtual elevation data to simultaneously estimate rolling resistance and aerodynamic drag [9]

- The instrumented bicycle isolates rolling resistance through the power balance equation by measuring and accounting for all other resistive forces directly [10]
- The coast-down method derives rolling resistance and drag from the deceleration recorded after the rider stops pedalling [11]
- The Hill method places an eccentrically weighted wheel on the road surface and derives the rolling resistance coefficient from the decay of the resulting pendulum oscillation [12]

Direct methods measure the resistive force at the tyre contact patch:

- Drum testing presses the tyre against a rotating steel cylinder in a controlled laboratory environment [13]
- Flat belt testing adapts this principle using a flat surface to avoid the curvature artefacts introduced by a drum [14]
- The tyre trailer measures resistance on actual road surfaces using a force transducer mounted in a purpose-built trailer towed at constant speed [15]

A further category of methods targets rolling impedance specifically: acceleration measurements quantify vibration levels at the rider–bicycle contact points via RMS or RMQ values, while the absorbed power method measures the force and velocity at the saddle and handlebars simultaneously to determine how much vibrational energy the rider's body actually absorbs Lépine et al. [6].

Each of these approaches involves a trade-off between controllability and realism. Outdoor and trailer-based methods preserve realistic surface conditions but cannot isolate the contribution of a single variable. Drum and flat belt setups offer repeatability and speed control but cannot reproduce an arbitrary road surface texture. None of the existing laboratory methods combines a replaceable, geometrically faithful road surface with a direct force measurement capable of characterising vibrational power loss as a function of both speed and tyre pressure. Lépine et al. [6], Dijkstra [16] and Fernández [5] all identify the need for a controlled, repeatable measurement setup that can isolate the effect of road surface texture on power loss and vibration transmission, including measurements with instrumented dummies to eliminate the variability introduced by human riders.

This thesis responds to that need by designing, building, and validating such an apparatus.

1.2. Theory

1.2.1. Forces acting on a bicycle

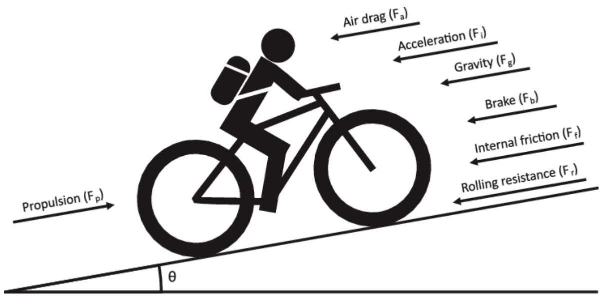

Figure 1.1: Forces on a bicycle [10]

The total resistive force acting on a moving bicycle can be decomposed into several components. Aerodynamic drag opposes the motion of the bicycle and rider through the air and scales with the square of velocity, making it the dominant resistance at higher speeds. Gravitational forces act when riding on a gradient, adding or reducing the required propulsive force depending on the slope direction. Braking forces are applied intentionally by the rider and are not considered here. Internal friction arises from the drivetrain (bearings, chain, and derailleur) and dissipates a small fraction of the propulsive power before it reaches the contact patch. Finally, rolling resistance acts at the tyre contact patches and arises from energy dissipation in the tyre material as it deforms and recovers under load. Together these forces determine the total power a cyclist must produce to maintain a given speed [10].

At cycling speeds below approximately 3 m/s, rolling resistance is the dominant resistive force, while aerodynamic drag becomes the dominant term at higher speeds [7]. To put these magnitudes in perspective: for a bicycle-plus-rider mass of 80 kg, C_{rr} values between 0.002 and 0.010 on a smooth, hard surface produce a rolling drag of 1.5 N to 7.8 N (15 W to 78 W at 10 m/s), while aerodynamic drag in low-wind conditions at typical riding speeds ranges from approximately 5 N to 30 N (50 W to 300 W at 10 m/s) [7]. In a laboratory setting with a stationary bicycle on a treadmill, aerodynamic drag is absent and the drivetrain is not driven, leaving rolling resistance as the only active resistive mechanism. Wheel bearing losses are present but Wilson and Schmidt [7] notes that these constitute a negligible fraction of the total resistance and can therefore be disregarded. This makes the treadmill apparatus well suited to studying the effect of road surface and tyre pressure on rolling resistance in isolation.

1.2.2. Rolling resistance

Rolling resistance arises primarily from hysteretic energy loss in the tyre material [2], [17]. As the tyre deforms at the contact patch and recovers after leaving it, the viscoelastic rubber dissipates a fraction of the deformation energy as heat [1]. The classical model expresses the rolling resistance force as:

$$F_{rr} = C_{rr} \cdot N \tag{1.1}$$

where C_{rr} is the dimensionless rolling resistance coefficient and N is the normal force at the contact patch [17]. In this model C_{rr} is treated as a constant, making F_{rr} independent of speed and proportional only to the normal load. In practice C_{rr} has a weak dependence on speed due to increased deformation frequency at higher speeds, but this effect is small within the speed range relevant to cycling [1].

1.2.3. Vibrational losses

On rough road surfaces, the tyre and bicycle are continuously excited by surface irregularities, generating vibrations that propagate through the bicycle frame and into the rider's body [4], [7]. This vibrational excitation dissipates additional energy beyond the classical rolling resistance term described in Equation 1.1, a component referred to here as vibrational loss F_{VL}. The total resistive force acting on the bicycle therefore combines both components [18]:

$$F_{TR} = C_{rr} \cdot N + F_{VL} \tag{1.2}$$

Unlike classical rolling resistance, vibrational power loss depends on multiple variables. Louhghalam et al. [3] show analytically that vibrational energy loss scales linearly with speed and quadratically with the frequency response function of the bicycle-rider system. This means that both surface roughness and the dynamic properties of the bicycle and rider have a disproportionately large influence on vibrational power loss. Fernández [5] confirmed this experimentally, finding a quadratic relationship between vibrational power loss and speed on rough surfaces, and showing that tire pressure and rider posture both affect the magnitude of vibrational losses. Lépine et al. [6] further demonstrated that rider posture alone produces substantially different frequency response functions between the road surface and the rider's body, meaning that two riders on identical equipment can experience significantly different vibrational power losses on the same surface.

An important consequence of combining classical rolling resistance and vibrational power loss is that an optimal tyre pressure is hypothesised to exist that minimises total power loss. As tyre pressure increases, classical rolling resistance decreases due to reduced tyre deformation at the contact patch. However, a stiffer tyre transmits more surface-induced impacts into the bicycle and rider, increasing vibrational power losses. The balance between these two competing effects is expected to produce a minimum in total power loss at an intermediate pressure, as illustrated in Figure 1.2.

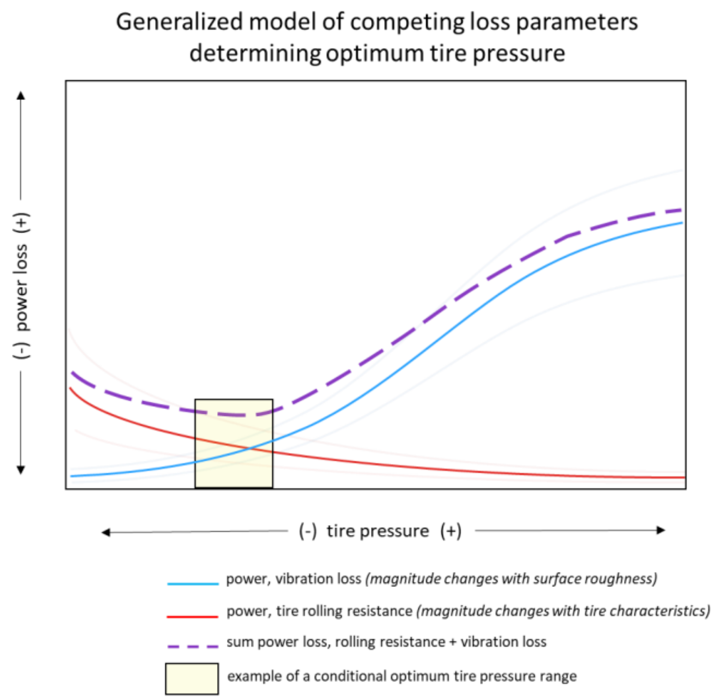

Figure 1.2: Hypothesised total power loss as a function of tyre pressure, showing the competing contributions of classical rolling resistance and vibrational loss and the resulting optimal pressure. Figure produced by SRAM Corporation [18]; note that this is a conceptual model from a commercial source and has not been independently validated.

The dependence of vibrational power loss on surface roughness, speed, tire pressure and rider posture motivates a measurement apparatus in which all of these variables can be controlled independently. This is the central design requirement of the apparatus developed in this thesis.

1.2.4. Road surface characterisation

Road surface roughness is the primary driver of vibrational excitation in a bicycle, and quantifying it correctly is essential for comparing surfaces and predicting power loss. Three main characterisation frameworks are used in the literature.

The International Roughness Index (IRI) is the global standard for expressing road roughness as a single scalar value. It is computed by simulating a quarter-car model travelling at 80 km/h over a measured road profile and accumulating the relative displacement between the sprung and unsprung masses [19]. While widely adopted, IRI was developed for motor vehicles and is dominated by long-wavelength roughness, making it a poor descriptor of surfaces relevant to cycling.

The Power Spectral Density (PSD) provides a more complete description by decomposing the road profile into its spatial frequency components, revealing how roughness energy is distributed across wavelength scales [20]. This spectral content provides a mechanistic link between surface wavelength, vibration frequency, and energy dissipation that IRI cannot. The ISO 8608 standard formalises this approach by approximating the full PSD with a power-law function, characterised by a single roughness coefficient $G_q(n_0)$ at a reference spatial frequency $n_0 = 0.1\,\mathrm{m}^{-1}$. Road surfaces are then classified into eight roughness classes (A–H) based on the value of $G_q(n_0)$, ranging from high-quality highways (Class A) to extremely rough terrain (Class H) [20].

The Bicycle Roughness Index (BRI) adapts the IRI quarter-car framework to bicycle dynamics by replacing the car parameters with bicycle-specific values and reducing the reference speed to approximately 15 km/h [21]. As a result, BRI is more sensitive to shorter wavelength irregularities in the megatexture range (50–500 mm), which are the primary source of vibrational excitation for cyclists. Typical road surfaces have BRI values around 40, while deliberately rough experimental surfaces can reach values of 160 or higher [5].

1.3. Research objective

The objective of this thesis is to design and validate a laboratory measurement apparatus capable of measuring the powerloss experienced by a cyclist on a controlled road surface. This apparatus is intended to be modular and extensible, serving as a platform for future research into vibration transmission from road surface to cyclist. The scope of this thesis is limited to performance-oriented measurements on a single klinker road surface (klinker is the dutch word for road brick and will be used throughout this thesis), characterising the effect of tire pressure and speed on rolling resistance and powerloss. This leads to the following research question:

> *What is the design of a measurement apparatus capable of measuring the powerloss experienced by a cyclist on a variable roughness road surface with quantified accuracy, and what is the effect of tire pressure and speed on powerloss for a klinker surface?*

1.4. Thesis structure

Chapter 2 describes the design of the measurement apparatus, including the force measurement system, road surface and stabilization mechanism. Chapter 3 describes the experimental method and data analysis procedure. The results are presented in chapter 4, followed by a discussion in chapter 5 and conclusions in chapter 6.

2
Design of Measurement Apparatus

In order to measure the powerloss experienced by a cyclist on different road roughness surfaces, a measurement apparatus is developed in this thesis. The apparatus is designed with two main objectives in mind. The primary objective is to measure the powerloss of a cyclist on a controlled road surface, isolating the effect of road surface and tire pressure from other variables such as wind that cannot be controlled outdoors [16]. The second objective is to provide a modular and extensible platform for future research. Follow-up studies include identifying how road-induced vibrations propagate through the bicycle and into the rider's body, and how this affects human health. These future research directions place additional demands on the apparatus, particularly regarding vibration measurement capability, and have therefore been incorporated into the design requirements from the outset.

The apparatus is built around a commercially available treadmill, which provides the controlled belt speed needed to drive the bicycle tyre without requiring the rider to pedal. All other components of the apparatus, including the road surface, the force measurement system, and the stabilization mechanism, are designed to integrate with this treadmill.

This chapter describes the design process and final design of the measurement apparatus. section 2.1 introduces the design methodology followed throughout this chapter. section 2.2 describes the design of the force measurement system. Section 2.3 describes the design of the road surface. Section 2.4 describes the design of the stabilization mechanism. Section 2.5 discusses the placement of the sensors within the system. Section 2.6 describes the instrumentation and data acquisition chain, including the uncertainty analysis. Finally, section 2.7 presents the completed apparatus.

2.1. Design Methodology

The apparatus consists of three main components, each of which involves an independent design decision: the power loss measurement system, the road surface, and the bicycle stabilization mechanism. Each component is designed following the same two-step process. First, a set of functional requirements is defined that the design must satisfy as a binary pass/fail condition, concepts that fail any requirement are eliminated. Second, the surviving concepts are evaluated against a set of design criteria using a three-level relative scoring system: good (+), neutral (○), or poor (−). The concept scoring best against the criteria is then selected.

2.2. Design of Measurement Apparatus

The core measurement objective of this measurement apparatus is to determine the power loss due to rolling resistance for a bicycle tire rolling on a given surface. This section describes the requirements and design criteria specific to the measurement system, followed by three conceptual approaches and their evaluation.

2.2.1. Requirements and design criteria

Requirements

The following requirements apply specifically to the power loss measurement system:

- The system must be capable of measuring the power loss due to rolling resistance.
- The bicycle must not be structurally modified.
- The system must be able to accommodate different types of bicycles without requiring changes to the bicycle itself.

Design criteria

The following four criteria are used to evaluate the surviving concepts on a relative scale: good (+), neutral (○), or poor (−).

Table 2.1: Design criteria for measurement apparatus.

Criterion	**Description**
Low measurement uncertainty	The concept should minimise the number of independent measurements that contribute to the final result.
Modifications needed to the bike and treadmill	The fewer modifications are needed to the treadmill and bike, the easier it is to integrate a system that fits both.
Ease of calibration	The concept should require as few calibration steps as possible. Each sensor or device in the measurement chain must be individually calibrated, reducing complexity and potential error sources.
Repeatability	The concept should produce consistent results under identical conditions. Concepts that depend on human input such as pedalling are inherently less repeatable than fully controlled mechanical systems.

2.2.2. Concept 1 --- Power pedals

The first concept uses power pedals mounted on the bicycle to measure the mechanical power input at the crank. By simultaneously measuring the power absorbed by the treadmill motor, which acts as a generator, the powerloss can be calculated as the difference between the two:

$$P_{loss} = P_{pedals} - P_{treadmill} \tag{2.1}$$

2.2.3. Concept 2 --- Electric motor drive

The second concept replaces the cyclist with a small electric motor mounted on the bicycle to drive the rear wheel at a controlled speed. The power input to the motor is then compared with the power consumed by the treadmill motor:

$$P_{loss} = P_{motor} - P_{treadmill} \tag{2.2}$$

This approach offers better repeatability than Concept 1 since the input power is controlled rather than human-driven. However, drivetrain losses between the motor and the tire contact patch introduce an additional source of uncertainty.

2.2.4. Concept 3 --- Direct force measurement

The third concept measures the rolling resistance force directly using a loadcell, without any modification to the bicycle or the treadmill. The bicycle is connected via a loadcell to a rigid frame while the treadmill belt moves underneath the tire at a controlled speed. The rolling resistance acts as a horizontal drag force in the direction of belt travel, which is measured directly by the loadcell. The power loss is then calculated as:

$$P_{loss} = F_{loadcell} \cdot v_{belt} \tag{2.3}$$

where $F_{loadcell}$ is the rolling resistance force [N] and v_{belt} is the treadmill belt speed [m/s].

2.2.5. Concept selection

All three concepts are first evaluated against the requirements defined in section 2.2. As shown in Table 2.2, all three concepts satisfy all requirements and the selection therefore proceeds to the design criteria.

Table 2.2: Requirements review for measurement apparatus.

Requirement	C1	C2	C3
Capable of measuring power loss	✓	✓	✓
No structural modification to bicycle	✓	✓	✓
Accommodates different bicycle types	✓	✓	✓
No permanent changes to treadmill	✓	✓	✓

The three surviving concepts are then scored against the design criteria, as shown in Table 2.3.

Table 2.3: Design criteria scoring for measurement apparatus.

Criterion	C1	C2	C3
Low measurement uncertainty	$-$	$-$	$+$
Modifications needed to the bike and treadmill	$-$	$-$	$+$
Ease of calibration	$-$	$-$	$+$
Repeatability	$-$	$\circ$	$+$

Concept 3 scores best overall and was therefore selected. On measurement uncertainty, concepts 1 and 2 both measure power loss from the difference between two independently measured power values. In Concept 1, additional drivetrain losses between the pedals and the tire contact patch are difficult to predict and quantify, adding uncertainty to the result. In Concept 2, the treadmill motor is required to act as a generator, a mode of operation it is not designed for, making accurate power measurement unreliable. Concept 3 avoids both of these issues by measuring the rolling resistance force directly with a single loadcell and multiplying by the belt speed, keeping the measurement chain short and well-defined.

For modifications to the bike and treadmill, Concept 1 requires the treadmill motor to be converted to operate as a generator, which is a significant modification to the existing treadmill. Concept 2 is worse still, as it additionally requires the bicycle to be modified to host the electric drive motor. Concept 3 requires no modifications to either the bicycle or the treadmill.

Calibrating electric motors is inherently difficult, particularly when they are required to operate outside their designed purpose as in Concepts 1 and 2. A loadcell as used in Concept 3 is straightforward to calibrate using known reference weights, making it the least complex option in terms of calibration.

Concept 3 is fully repeatable, since the measurement depends only on the load cell and belt speed, both of which are stable and controllable. Concept 2 scores neutrally because although the electric motor provides a controlled input, the drivetrain losses between the motor and the tire contact patch are difficult to predict and may vary between trials. Concept 1 scores poorly since the pedaling force depends on the human operator, introducing variability between measurements.

2.3. Design of roadsurface

2.3.1. Requirements and design criteria

The road surface must represent a real-world cycling surface while remaining physically compatible with the treadmill. The following requirements and design criteria govern the design of the road surface.

Requirements

The following requirements apply specifically to the road surface:

- The surface must be geometrically representative of a real-world cycling surface.
- The surface must not damage or permanently deform the treadmill belt.
- The surface must remain fixed relative to the treadmill belt during measurement, without shifting (so the roadsurface is the same every revolution).
- The surface must be replaceable, allowing different surfaces to be tested on the same apparatus without modification to the treadmill.
- A speed of 30 km/h needs to be achieved on the roadsurface by the cyclist.
- The roadsurface needs to withstand a vertical load of 100kg while spinning at 30 km/h.

Design criteria

The following four criteria are used to evaluate the surviving concepts on a relative scale: good (+), neutral (○), or poor (–).

Table 2.4: Design criteria for road surface.

Criterion	Description
Surface fidelity	The manufactured surface should reproduce the geometry of the real road surface as accurately as possible. Deviations in texture or profile directly affect the rolling resistance measurement.
Ease of manufacturing	The surface should be producible with available equipment and within a reasonable timeframe. Complex manufacturing processes increase lead time and limit the number of surfaces that can be produced.
Replaceability	Switching between surfaces should require minimal effort and no modification to the treadmill. A surface that is difficult to swap reduces the practical usability of the measurement apparatus.
Muliple surface	One concept should allow muliple types of roadsurfaces, so the same production method can be used, to simplify the production of new roadsurfaces.
Structural integrity	The surface must remain rigid and undamaged under repeated loading from the bicycle tyre. Deformation or wear of the surface over time would introduce variability between measurements.

2.3.2. Concept 1 --- 3D scanned surface

The first concept reproduces the road surface geometry by 3D scanning actual klinker bricks in the field using a professional handheld 3D scanner. The scanner captures the surface as a dense point cloud, which is processed into a closed triangular mesh and subsequently 3D printed in PLA. The printed bricks are glued onto aluminium slabs, which are bolted directly to the treadmill slats. This two-layer attachment ensures that muliple orientations of the scanned bricks can be made, such as fishtail and horizontal orientation.

The key advantage of this concept is geometric fidelity. Because the surface geometry is captured directly from real bricks, all surface features (including broken edges, cracks and surface texture), are reproduced as they exist in the real world.

2.3.3. Concept 2 --- Mathematically defined surface

The second concept replaces the scanned geometry with a mathematically defined surface. Rather than reproducing real brick geometry, rectangular slabs of uniform dimensions are used to approximate the roadsurface, similiar to [5]. A real road surface is scanned and the pseudo PSD is formed by changing the spacing between the rectangular slabs.

This concept is easier to manufacture since it doesnt require the scanning of individual bricks, meshing them and printing many individual bricks. However, there is a limitation in spacing since the treadmill has a set belt length.

2.3.4. Concept selection

All concepts are first evaluated against the requirements. As shown in Table 2.5, both concepts satisfy all requirements and neither is eliminated at this stage. The final selection is therefore based on the design criteria.

Table 2.5: Requirements review for road surface.

Requirement	C1	C2
Geometrically representative of real surface	✓	✓
Does not damage treadmill belt	✓	✓
Remains fixed during measurement	✓	✓
Replaceable without treadmill modification	✓	✓
A speed of 30 km/h needs to be reached by the cyclist	✓	✓
The cyclist needs to withstand a vertical load of 100kg while spinning at 30 km/h	✓	✓

Table 2.6: Design criteria scoring for road surface.

Criterion	C1	C2
Surface fidelity	$+$	$-$
Multiple surfaces possible	$+$	$-$
Ease of manufacturing	$-$	$+$
Replace ability	$\circ$	$\circ$
Structural integrity	$\circ$	$+$

Concept 1 was selected on the basis of surface fidelity and the possibility of having multiple surfaces. The primary purpose of the road surface in this setup is to reproduce the rolling resistance characteristics of a real klinker surface as accurately as possible. A mathematically defined surface can approximate the macroscopic brick pattern but cannot capture the natural height variation between bricks, worn edges, or surface roughness that are inherent to real klinkers and directly influence the tyre contact mechanics. Concept 1 reproduces these features by construction. Although Concept 1 requires more manufacturing effort due to the scanning and mesh processing pipeline, this is a one-time cost per surface type and does not affect measurement quality once the surface is produced.

2.3.5. Final roadsurface design

The final road surface is built from 6 individually scanned klinker bricks. Each brick was scanned on both of its two opposing faces, yielding 12 unique surface scans in total. Each scan can additionally be mounted in two orientations by rotating the brick $180°$ around the vertical axis, so that the tyre contacts either the original or the flipped face of the same brick. This gives a total of 24 distinct surface configurations from a single set of 6 bricks, providing a wide range of surface variation for future measurements without requiring additional scanning or manufacturing. T

Scanning

Each brick was placed on a turntable and scanned using a professional handheld 3D scanner, as shown in Figure 2.1. The scanner projects structured light onto the surface and captures the reflected geometry as a dense point cloud. Both faces of each brick were scanned separately. The resulting point clouds were processed to remove noise and merged into a single watertight mesh per face using Meshmixer, where mesh errors and non-manifold geometry were repaired to produce a clean solid body.

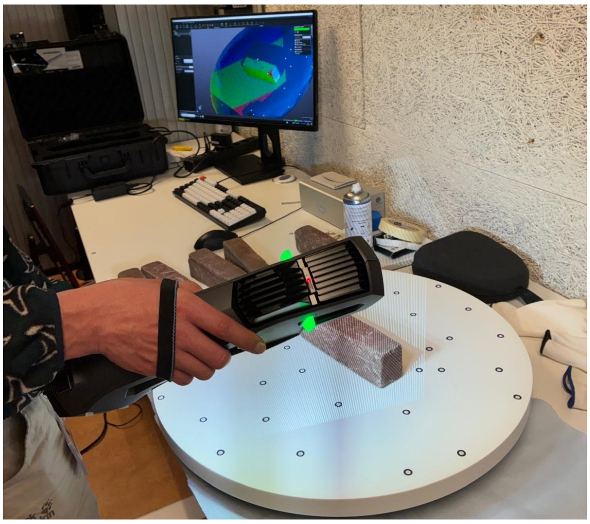

Figure 2.1: Handheld 3D scanning of a klinker brick on a turntable. The point cloud is visible in real time on the monitor in the background.

CAD file

The repaired mesh was exported as an OBJ file and imported into Meshmixer, where it was converted into a printable solid. The model was then sliced in SolidWorks and exported for FDM printing. The resulting CAD geometry, shown in Figure 2.2, reproduces the surface texture, edge wear and cracks of the original klinker. The bricks were printed in PLA on a Bambu Lab X1-carbon printer. PLA was selected for its low cost and wide availability, layersize was 0.2mm, the accuracy of the printer is 200 μm.

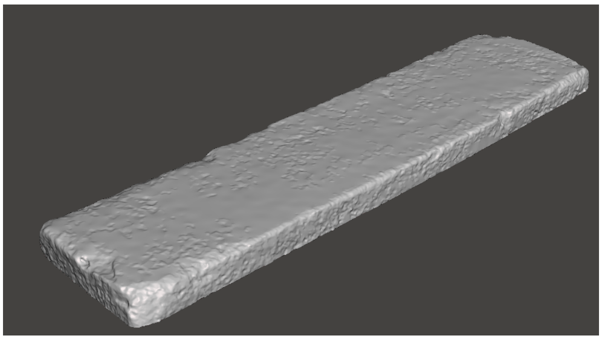

Figure 2.2: Rendered CAD model of a scanned klinker brick after mesh repair and slicing. The surface texture and edge geometry of the original brick are clearly visible.

2.3.6. Complete assembly

The measurement apparatus is built around a Technogym Skill Run treadmill. Unlike conventional treadmills, which use a single continuous rubber belt, the Skill Run uses a slatted belt construction in which individual rigid slats are connected by a continuous loop, as shown in Figure 2.3. Each rubber slat has a vertical crossbeam on its underside to provide structural rigidity, as visible in Figure 2.4. This slatted construction was selected specifically because it allows mimicked road surface to be bolted directly on top of the individual rubber slats, keeping them fixed relative to the belt during measurement and making them straightforward to replace between test configurations without any permanent modification to the treadmill.

Figure 2.3: Top view of the Technogym Skill Run slatted belt, showing the individual rubber slats connected by a continuous loop.

(a) Bottom view of a single rubber slat, showing the vertical crossbeam.

(b) Side view showing the rubber slat and its crossbeam.

(c) Side view showing the aluminium slat bolted on top of the rubber slat.

Figure 2.4: Close-up views of a single treadmill rubber slat and the aluminium slat mounted on top of it.

Each printed brick is glued onto an aluminium slat. The aluminium slat is then bolted on top of the rubber treadmill slat through pre-drilled holes, as shown in Figure 2.5. This two-layer attachment ensures that each brick remains rigidly fixed to the belt during measurement and cannot shift or vibrate independently.

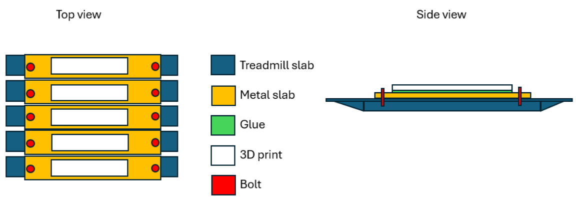

Figure 2.5: Schematic overview of the road surface assembly, showing the relationship between the printed brick, aluminium slat and treadmill slat.

The complete assembled road surface, covering the full width of the treadmill, is shown in Figure 2.6.

During initial testing, the aluminium slats were found to deflect excessively at the point where the belt transitions around the treadmill rollers, where the slat accelerates from the underside back to the top surface. This deflection caused the slats to strike the rubber treadmill slabs hard at each transition. Zipties were therefore added along the outer edges of each printed brick to constrain this deflection and eliminate the impact. All the iterations of the roadsurfaces can be found in Appendix D.

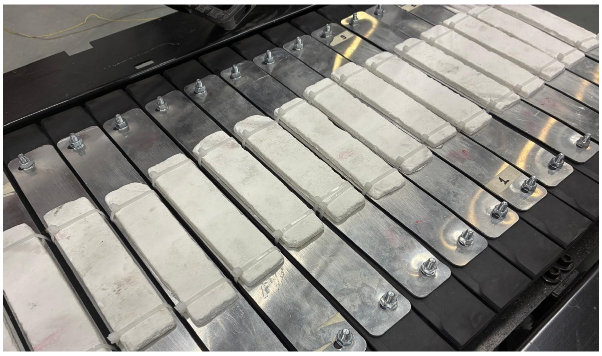

Figure 2.6: Complete road surface assembled on the treadmill, showing all bricks mounted across the full belt width.

2.4. Design of stabilization mechanism

During a trial, the bicycle must remain in a controlled and repeatable position relative to the treadmill. Without a stabilization mechanism, two practical problems arise. First, a human rider may gradually drift or begin steering during a measurement, particularly over longer test durations. Any lateral or yaw motion of the bicycle changes the contact geometry between the tire and the belt, introducing a tire deformation component that is unrelated to the road surface under investigation. Since the goal of this thesis is to isolate the effect of road surface texture on rolling resistance, this source of variability must be eliminated. Second, future research on this measurement apparatus is intended to use an instrumented dummy in place of a human rider. Unlike a human, a dummy cannot actively balance or steer, making a passive stabilization mechanism a strict necessity for this use case.

The stabilization mechanism must therefore constrain the degrees of freedom that would affect the measurement, while leaving free those that are physically necessary for the tire to roll naturally. Specifically, yaw, roll, and lateral motion must be constrained, while pitch, longitudinal and vertical motion remain free. It should be noted that the mass of the stabilization mechanism introduces an additional vertical load on the tyrea beyond what the rider alone would generate, which increases the rolling resistance at the contact patches. This effect is discussed further in subsection 5.1.2. Another important consequence of any stabilization mechanism is that it introduces a longitudinal force component into the system, regardless of concept. The placement of the loadcell to account for this effect is discussed in section 2.5.

2.4.1. Requirements and design criteria

Requirements

The following apply specifically to the stabilization mechanism:

- The mechanism must constrain yaw, roll, and lateral motion of the bicycle while leaving pitch, longitudinal and vertical motion free.
- The mechanism must accommodate bicycle handlebar widths ranging from 240 mm to 780 mm and wheel diameters ranging from 24 inch to 29 inch.
- The mechanism must not permanently or structurally modify the bicycle.
- The mechanism must withstand a roll moment force of at least 100 Nm, corresponding to the maximum roll moment a rider can exert during a measurement.

- The mechanism must not introduce a measurable force in the longitudinal direction, as this directly affects the loadcell reading.

Design criteria

The following criteria are used to evaluate the surviving concepts on a relative scale: good (+), neutral (○), or poor (−).

Table 2.7: Design criteria for stabilization mechanism.

Criterion	**Description**
Number of joints	Each additional joint introduces play and potential friction. Minimising the number of joints reduces cumulative imperfections and their effect on the free degrees of motion.
Joint friction in free directions	Friction in joints that should allow free motion (pitch, vertical, and longitudinal movement) should be as little as possible. Unnecessary friction will restrict the natural movement of the bike and negatively influence the rolling resistance measurement.
Stiffness in constrained directions	The mechanism must be sufficiently rigid in the directions it constrains: yaw, roll, and lateral. Play or bending in these direction should be as limited as possible.
Mass of mechanism	The mass of the mechanism adds to the total load on the tire and changes the dynamic response of the bicycle. A lighter mechanism minimizes its influence on the rolling resistance measurement.
Ease of mounting different bicycles	The mechanism should allow a different bicycle to be mounted quickly and without extensive adjustment. A complex or bicycle-specific mounting procedure increases test preparation time and the risk of inconsistent positioning between trials.
Connection point robustness	The connection between the mechanism and the bicycle must reliably handle rider-induced loads without risk of slipping or damaging the bicycle. The connection point must be structurally suitable for lateral and vertical loads.

2.4.2. Concept 1 --- Two-bar linkage at the front fork

The first concept uses a two-bar linkage on each side of the bicycle, connected to the front fork via a hinge joint, as shown in Figure 2.7. Each linkage consists of two links and three hinge joints, one fixed to the treadmill frame, one intermediate joint, and one connecting to the front fork. The two linkages on either side are connected by crossbeams. The in-plane motion of each two-bar linkage allows pitch, vertical, and longitudinal movement, while the double-sided structure with crossbeams restricts roll, yaw, and lateral motion.

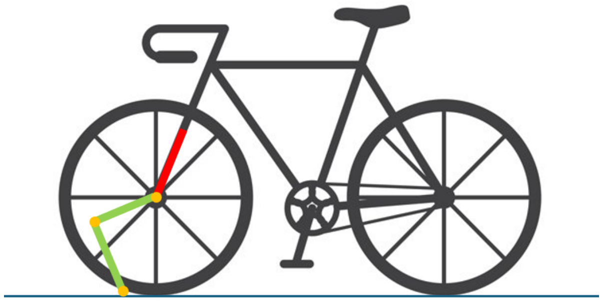

Figure 2.7: Concept 1: Two-bar linkage connected to the front fork. Yellow dots indicate hinge joints. Green links form the two-bar linkage, red link connects to the front fork.

2.4.3. Concept 2 --- Cantilever beams with sliding joint at the handlebars

The second concept uses two vertical cantilever beams, one on each side of the bicycle, connected to the handlebars via a sliding joint, as shown in Figure 2.8. The sliding joint allows vertical motion, while the cantilever beam allows for longitudinal movement. On the sliding a joint an additional hinge joint is located to enable pitch movement. The two beams are connected by crossbeams, restricting roll, yaw, and lateral motion. In the constrained directions, the beams act as rigid cantilevers, resisting lateral and yaw loads through their bending stiffness.

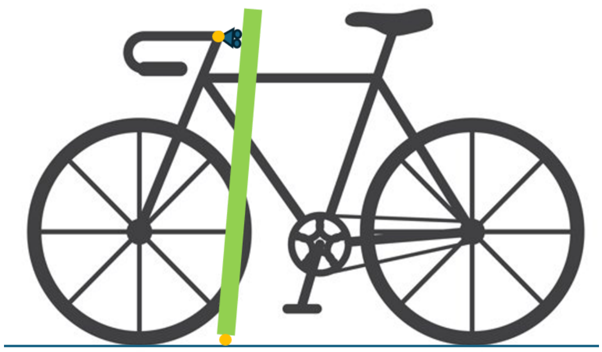

Figure 2.8: Concept 2: Cantilever beams with sliding joint at the handlebars. Yellow dots indicate hinge joints, blue indicates the sliding joint. Green beam is the cantilever member.

2.4.4. Concept 3 --- Two-bar linkage at the handlebars

The third concept is kinematically identical to Concept 1,using a two-bar linkage on each side of the bicycle connected by crossbeams. The key difference is the connection point, instead of the front fork, the mechanism connects to the handlebars via a hinge joint, as shown in Figure 2.9. The handlebar connection is more universal across different bicycle types and is structurally better suited to handling the lateral and vertical loads compared to the front fork.

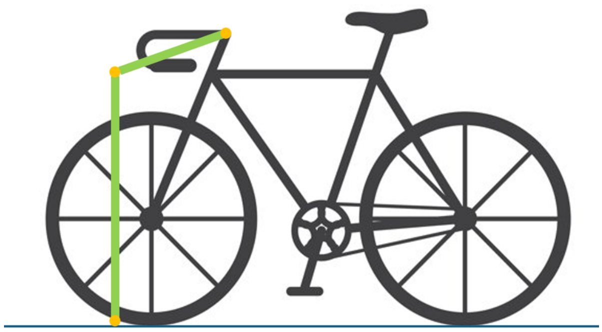

Figure 2.9: Concept 3: Two-bar linkage connected to the handlebars. Yellow dots indicate hinge joints. Green links form the two-bar linkage.

2.4.5. Concept selection

All three concepts are first evaluated against the requirements. As all three concepts satisfy the requirements, none is eliminated and the selection proceeds to the design criteria.

Table 2.8: Requirements review for stabilization mechanism.

Requirement	C1	C2	C3
Constrains yaw, roll, lateral; free in pitch, longitudinal, vertical	✓	✓	✓
Accommodates different bicycle sizes	✓	✓	✓
No permanent modification to bicycle	✓	✓	✓
Withstands lateral rider forces	✓	✓	✓
No measurable longitudinal force introduced	✓	✓	✓

The three surviving concepts are scored against the design criteria in Table 2.9.

Table 2.9: Design criteria scoring for stabilization mechanism.

Criterion	C1	C2	C3
Number of joints	○	○	○
Joint friction in free directions	+	−	+
Stiffness in constrained directions	○	+	○
Mass of mechanism	+	○	○
Ease of mounting different bicycles	−	○	○
Connection point robustness	−	○	○

Concept 3 scores best, scoring neutral on all criteria with one positive score, making it the most consistent concept overall, and was therefore selected.

Concept 1 scores well on mass since its linkage connects low on the bicycle, requiring shorter members. However, it scores poorly on both ease of mounting and connection point robustness. Connecting to the front fork requires bicycle-specific adaptation, as fork geometries vary significantly between bicycle types. Furthermore, carbon front forks (common on road bicycles) are not designed to handle the lateral loads imposed by the stabilization mechanism, creating a risk of damage.

Concept 2 scores well on stiffness in the constrained directions, as the cantilever beams resist lateral and yaw loads through their own rigidity without relying on joint stiffness. However, it scores poorly on joint friction in the free directions. The sliding joint connecting the handlebars to the cantilever beam introduces friction in the vertical direction, which resists the natural vertical motion of the bicycle during rolling. More critically, sliding joints are prone to stick-slip behaviour, a phenomenon where static friction temporarily locks the joint before it suddenly releases. If the sliding joint jams, the vertical and pitch motion of the bicycle are restricted, which could damage the bicycle or the mechanism.

Concept 3 avoids both of these issues. By connecting to the handlebars rather than the front fork, it is compatible with a wide range of bicycle types without requiring adaptation, and the handlebar structure is well suited to handling lateral and vertical loads. By using only hinge joints rather than a sliding joint, it eliminates the risk of stick-slip behaviour. Although hinge joints introduce some friction, this friction acts in the rotational direction and is small and reliable compared to the stick-slip forces of a sliding joint. All three concepts introduce a longitudinal force component into the system due to the presence of the mechanism, this effect is addressed in the loadcell placement in section 2.5.

2.5. Sensor placement

The goal of the measurement system is to determine the total rolling resistance force acting on the bicycle. As established in section 2.4, the stabilization mechanism introduces a longitudinal force component into the system at the handlebar connection point. This force acts in the same direction as the rolling resistance force and is therefore measured by the main load cell if not accounted for separately. To correctly isolate the rolling resistance, both the main load cell force and the interface force must be measured independently.

2.5.1. Free body diagram

The free body diagram of the bicycle in the longitudinal direction is shown in Figure 2.10. Four horizontal forces act on the system. The rolling resistance forces at the front and rear tire contact patches, $F_{rr_{\text{front}}}$ and $F_{rr_{\text{rear}}}$, act in the direction of belt travel. These are opposed by two forces: the main load cell force F_m, which connects the bicycle to a fixed reference frame. Secondly, the interface force F_i, the longitudinal force introduced by the stabilization mechanism at the handlebar connection point. Although the bicycle is connected to a fixed reference frame, a small longitudinal displacement remains possible due to either a spring placed between the load cell and the bicycle, or slight elastic stretch in the rope connecting the load cell to the bicycle.

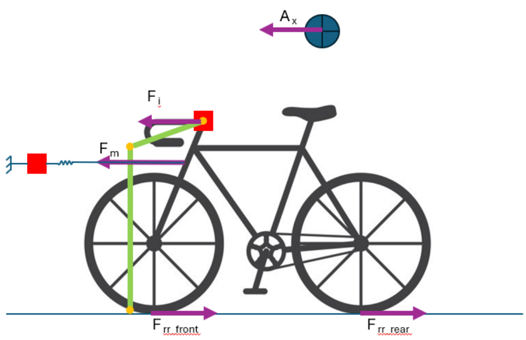

Figure 2.10: A free body diagram of all the forces acting on the bicycle in longitudinal direction. The red boxes represent the individual loadcells.

Applying Newton's second law in the longitudinal direction:

$$\sum F_x = F_{rr_{\text{front}}} + F_{rr_{\text{rear}}} - F_m - F_i = ma_x \tag{2.4}$$

This means that measuring only the main loadcell is insufficient; the interface force must also be measured and added to obtain the correct total resistive force. The two sensors share the reaction of the rolling resistance: if the stabilization mechanism pulls the bicycle forward at the handlebars (a positive F$_i$), it takes over part of the resistance that would otherwise be carried by the main loadcell, so the value of F_m drops by the same amount. The reverse is also true, when the mechanism pushes backward, F_m increases. In both cases the total resistive force is only recovered by summing the two. A dedicated sensor is therefore required at the handlebar connection point to measure F_i, so that both contributions are captured.

When the bicycle pitches, for example when rolling over a bump, the angles of both the interface force and the main loadcell rope deviate from the horizontal, introducing a cosine correction factor into the force balance equation:

$$\sum F_x = F_{rr_{\text{front}}} + F_{rr_{\text{rear}}} - F_m \cos(\Phi) - F_i \cos(\theta) = ma_x \tag{2.5}$$

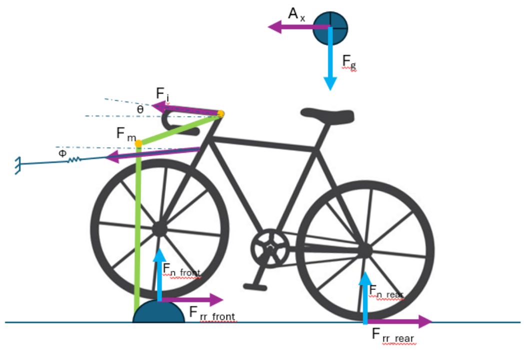

Figure 2.11: Free body diagram of the bicycle in the longitudinal direction during pitch. θ is the pitch angle of the stabilization mechanism and ψ is the angle of the main loadcell rope from horizontal.

where θ is the pitch angle of the stabilization mechanism and ψ is the angle of the main loadcell rope from horizontal. To assess the significance of this effect, a worst-case bump height of 2 cm is considered. With a bicycle wheelbase of 100 cm, the pitch angle of the bicycle is $\theta = \arctan(2/100) = 1.15$, giving $\cos(\theta) = 0.9998$. With a main loadcell rope length of 30 cm, the rope angle is $\Phi = \arctan(2/30) = 3.81$, giving $\cos(\Phi) = 0.9978$. Both cosine factors are within 0.02% and 0.22% of 1, meaning the pitch-induced error in the force measurement is negligible. The pitch motion of the bicycle can therefore be ignored in the force balance, and the equation from Equation 2.4 remains valid. A single-axis horizontal loadcell is therefore sufficient to measure the interface force. However, the vertical force at the connection point must still be prevented from influencing the loadcell, which is addressed in the flexure design in subsection 2.5.2.

2.5.2. Flexure design

To allow a single-axis loadcell to measure only the horizontal interface force without being influenced by the vertical force, a flexure is used. A flexure is a compliant mechanical element that achieves controlled motion through elastic deformation rather than sliding or rolling joints [22] . In this application, the flexure consists of two parallel thin plates oriented vertically. Under a horizontal load, the plates bend slightly, allowing a small longitudinal displacement δx, as can be seen in Figure 2.12. In all other directions (vertical translation, lateral translation, and rotation in pitch, roll and yaw) the two-plate configuration is effectively rigid, as any such motion would require one plate to extend and the other to compress simultaneously. The flexure therefore transmits vertical and lateral forces without displacement, meaning these force components are not transferred to the loadcell. Only the horizontal force component passes through to the loadcell, as can be seen in Figure 2.13.

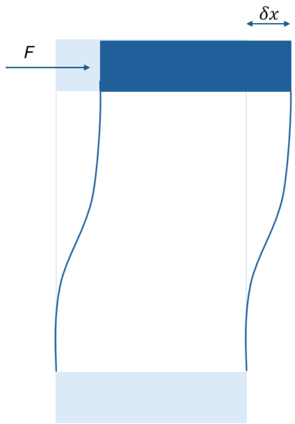

Figure 2.12: Explanation of the parallelogram flexure principle.

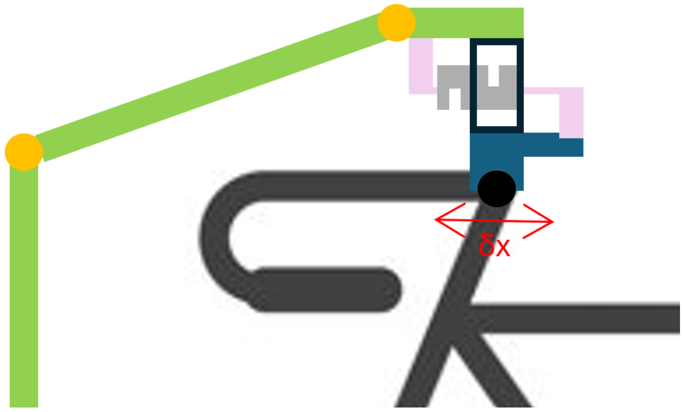

Figure 2.13: Schematic of the flexure assembly at the handlebar connection point. The green bars represent the beams of the stabilization mechanism, connected by yellow hinge joints. The blue component is the handlebar mount, the pink components are rod end bearings, the black trapezium represents the flexure, and the grey component represents the loadcell.

The flexure and load cell act as a parallel spring system between the handlebar and the stabilization mechanism, as shown in Figure 2.14. When a force is applied to this system, the total force is shared between the flexures and the load cell in proportion to their stiffnesses. To maximise measurement resolution, the load cell must be allowed to deflect through its full rated range under the expected loads. This requires the flexure to be significantly more compliant than the load cell: if the flexure were stiffer, it would carry the majority of the applied force and prevent the load cell from deflecting sufficiently, leaving only a small fraction of its rated range utilised and resulting in a poor signal-to-noise ratio. By designing the flexure to be more compliant than the load cell, the load cell deflects through its full range and the measurement resolution is maximised.

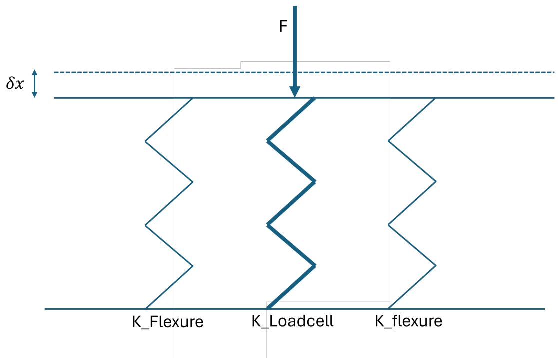

Figure 2.14: Schematic of the parallel spring system between the stabilization mechanism (top bar) and the handlebars (bottom bar). The applied force is distributed across two flexures and one loadcell. Since the flexures are significantly more compliant than the loadcell, the loadcell is free to deflect through its full rated range, maximising measurement resolution.

The loadcell used has a measurement range of 0–25 kg and a maximum deflection of 0.3 mm at full load. The flexure is therefore designed to deflect 1 mm under the same 25 kg load, making it approximately three times more compliant than the loadcell and ensuring the loadcell deflects through its full rated range. The loadcell was calibrated by applying known reference weights, confirming the linearity ($R^2 = 0.9996$) and sensitivity (0.0971 V/N) of the flexure/loadcell combination. More information on the calibration procedure can be found in Appendix B.

Two flexure devices are used in parallel at the handlebar connection point (one on the left side of the handlebars, the other on the right), each consisting of two parallel thin plates. The physical assembly is shown in Figure 2.15 and Figure 2.16. The vertical load at the handlebar connection point was estimated at 4 kg, representing the assumed fraction of the total 13 kg stabilization mechanism mass acting on the handlebars. This estimate was later verified by direct measurement, which yielded a value of 3.6 kg. Assuming a peak acceleration of 2 g and applying a safety factor of 2, this gives a vertical design load of 160 N at the connection point. The horizontal design load of 120 N was chosen such that the resulting flexure stiffness is significantly lower than that of the loadcell, ensuring the loadcell can deflect through its full rated range, while remaining sufficiently stiff to avoid excessive deformation under normal operating conditions. These loads are divided equally between the two flexure devices, giving 80 N vertical and 60 N horizontal per device.

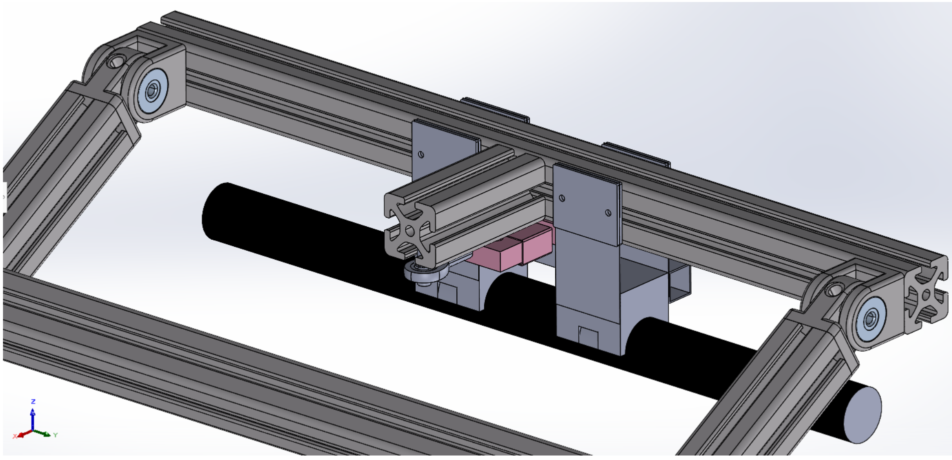

Figure 2.15: Top view of the flexure assembly at the handlebar connection point. The black tube represents the handlebar, the two outer components are the flexure devices, and the red component located between them is the loadcell.

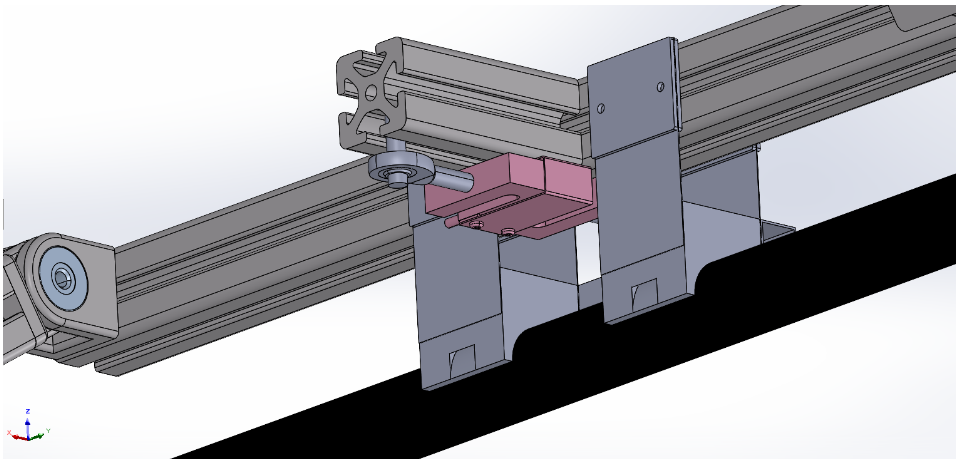

Figure 2.16: Bottom view of the flexure assembly at the handlebar connection point. The black tube represents the handlebar, the two outer components are the flexure devices, and the red component located between them is the loadcell.

Since the entire flexure and load cell assembly is connected to the handlebar mounts (blue mount in Figure 2.17a), the measurement is insensitive to the rotation of the handlebar clamp. If the clamp rotates around the handlebar tube during a measurement, any rotation acts about that single connection point. This is a degree of freedom the stabilization mechanism already accommodates through its hinge joint (the top hinge joint in Figure 2.13). The force measurement is therefore unaffected.

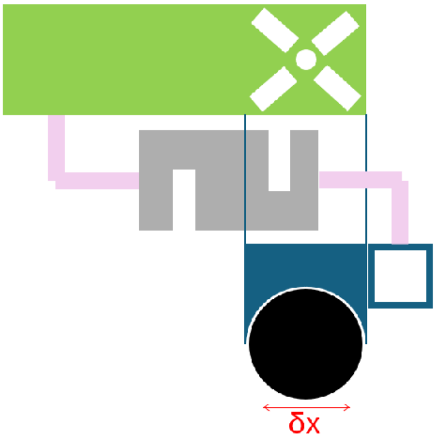

(a) Schematic of the flexure assembly. The green beams represent the stabilization mechanism, the black rectangle is the flexure, the blue spring represents the loadcell, and the red arrow indicates the allowed displacement δ_x.

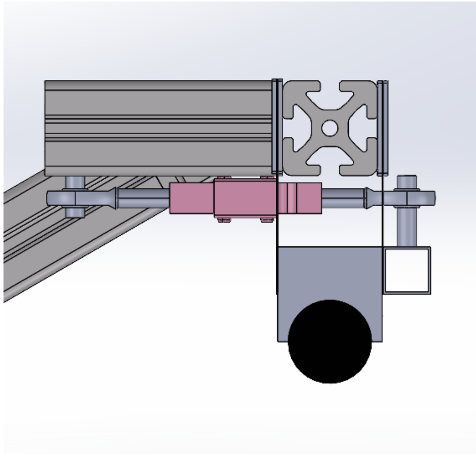

(b) Photograph of the flexure assembly from the same viewpoint as the schematic. The black circle is the handlebar, the red component is the loadcell, and the rod end bearings connecting the loadcell are visible on either side.

Figure 2.17: Flexure assembly at the handlebar connection point.

The schematic design of a single flexure device is shown in Figure 2.17a. The flexure is manufactured from steel DIN 1.4310, a stainless spring steel commonly used for flexure applications due to its high elastic limit and fatigue resistance. The material has a hardness of 230 HB and a fatigue strength of 300 MPa. A static and fatigue analysis was performed in SolidWorks to verify the design, as shown in Figure 2.18. The maximum von Mises stress under the combined loading condition is 250 MPa, which is below the fatigue limit of 300 MPa. The flexure is therefore designed for infinite fatigue life under the expected operating loads.

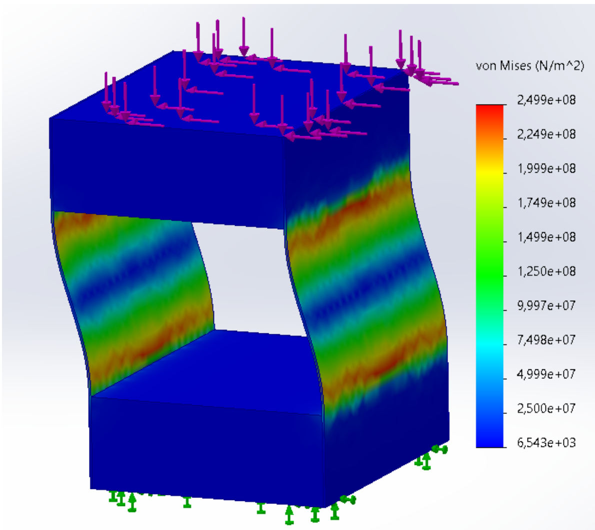

Figure 2.18: Flexure stress profile

A more extensive description of the flexure design, including dimensional drawings and full analysis results, is provided in Appendix A.

2.6. Instrumentation and data acquisition

The instrumentation setup consists of four sensors, two signal conditioners, and a data acquisition system. Two Scaime ZFA loadcells (scaime, Juvigny, France) are used to measure the forces in the system. One loadcell measures F_m and the other measures F_i via the flexure assembly. Both loadcells have a measurement range of 0–250N and are capable of operating in both compression and tension. The capability of measuring both compression and tension is particularly important for the interface loadcell, since forces occur in both directions. Each loadcell is connected to a dedicated Scaime CPJ strain gauge conditioner, which outputs a 0 to $\pm$10 V signal proportional to the applied load. An ADXL335 accelerometer is mounted on the handlebar stem to measure road-induced vibrations, additionally to measure longitudinal acceleration. The conditioned signals are recorded using a National Instruments USB-6009 data acquisition device (National Instruments, Austin, USA), which can sample all channels at 100 Hz and transfers the data to a laptop for processing. Data is stored in a CSV file using flexlogger (National Instruments, Austin, USA), software used to configure and use the NI USB-6009. The treadmill belt speed is read manually from the treadmill display in km/h and converted to m/s for use in the power loss calculation. A full overview of the sensor datasheets is provided in Appendix C.

The sampling rate of 100 Hz was selected based on the Nyquist criterion [23]. The relevant frequency range for rolling resistance measurements is primarily governed by the vibration-induced power loss model of Wilson and Schmidt [7], which identifies 9–50 Hz as the critical range for energy dissipation in cyclists. The 100 Hz sampling rate provides a Nyquist limit of 50 Hz, which is sufficient to capture this range. Higher frequency components associated with tire tread impacts (300–400 Hz) [24] are outside the scope of this measurement and are not captured. It should be noted that since each trial is reduced to a single mean value of F_{TR} over 60 seconds, the sampling rate does not need to resolve individual vibration cycles to achieve a stable mean. Fenre [10] shows that a 1 Hz sampling rate is sufficient to obtain a precise mean rolling resistance estimate provided enough samples are collected, with a precision of ±0.003 already achieved at 24 samples. A much lower sampling rate would therefore be adequate for the purpose of obtaining a stable mean. The 100 Hz rate was retained to preserve the time-resolved force signal for potential future analysis of dynamic load variations and vibration measurements.

2.6.1. Uncertainty analysis

The measurement uncertainty is evaluated following the *Guide to the Expression of Uncertainty in Measurement* (GUM) [25]. In this framework, every relevant source of uncertainty is identified, quantified as a standard uncertainty, and propagated into a single combined standard uncertainty for the measurand. The GUM distinguishes two ways of *evaluating* an uncertainty component, referred to as Type A and Type B. Both yield standard uncertainties and are treated identically once quantified.

Type A uncertainty

Type A uncertainty is evaluated statistically from a series of repeated measurements. It captures the random effects in the measurement chain, such as electrical noise and road-induced vibration, and is quantified here as the standard deviation of the mean of the repeated trials.

Type B uncertainty

Type B uncertainty is evaluated from sources of information other than repeated observation, primarily manufacturer specifications and calibration data. It captures the systematic effects of the instrumentation, such as sensor accuracy and resolution.

Manufacturer specifications typically quote a tolerance as a symmetric interval $\pm a$, for example a percentage of full scale. Such a figure is a bound: it states that the true value lies somewhere within $[-a, +a]$, but gives no information about where inside that interval it is more likely to fall. A standard uncertainty, by contrast, is a standard deviation, and the two cannot be combined until they are expressed in the same form. The bound must therefore first be converted into a standard uncertainty, which requires assuming a probability distribution across the interval. In the absence of any further information, a rectangular (uniform) distribution is assumed, reflecting that no value within the interval is considered more probable than another. The standard uncertainty is then the standard deviation of that distribution.

$$u_B = \frac{a}{\sqrt{3}}, \tag{2.6}$$

Combined standard uncertainty

The Type A and Type B components are combined into a single combined standard uncertainty u_c. Assuming the contributing sources are independent, they are combined as the root sum of squares:

$$u_c = \sqrt{u_A^2 + u_B^2}. \tag{2.7}$$

Expanded uncertainty

To report the result with a stated level of confidence, the combined standard uncertainty is multiplied by a coverage factor k to obtain the expanded uncertainty:

$$U = k\, u_c. \tag{2.8}$$

The measurement result is then expressed as $Y = y \pm U$. Assuming the output quantity is approximately normally distributed, the coverage factor corresponds to the confidence levels listed in Table 2.10.

Coverage factor k	Confidence level
1	68 %
2	95 %
3	99 %

Table 2.10: Coverage factor k and the corresponding confidence level for a normally distributed output quantity.

Type A - repeatability

The Type A uncertainty is evaluated statistically from a series of repeated measurements, following the method described by Papaioannou and Koulocheris [26]. Ten trials ($N = 10$) were conducted at 15 km/h with a 20 kg load under identical conditions. The standard uncertainty is then obtained through the following steps.

1. **RMS per trial** For each trial i, the root mean square of the rolling resistance signal is computed over its n samples.

$$Y_{\text{RMS},i} = \sqrt{\frac{1}{n}\sum_{j=1}^{n} F_{TR}^2}. \tag{2.9}$$

   The RMS is used as a representative measure of the signal magnitude because it captures both the mean level and the dynamic content due to road-induced vibrations.

2. **Mean RMS across 10 trials.** The 10 per-trial RMS values are averaged.

$$\bar{Y}_{\text{RMS}} = \frac{1}{N}\sum_{i=1}^{N} Y_{\text{RMS},i}. \tag{2.10}$$

3. **Standard deviation of the 10 RMS values** The sample standard deviation of the per-trial RMS values quantifies the trial-to-trial scatter.

$$\sigma_{Y_{\text{RMS}}} = \sqrt{\frac{1}{N-1}\sum_{i=1}^{N}\left(Y_{\text{RMS},i} - \bar{Y}_{\text{RMS}}\right)^2}. \tag{2.11}$$

4. **Standard uncertainty** Dividing by the square root of the number of trials gives the Type A standard uncertainty.

$$u_A = \frac{\sigma_{Y_{\text{RMS}}}}{\sqrt{N}}. \tag{2.12}$$

   This represents how much the RMS-mean result would be expected to vary if the entire set of trials were repeated.

The results are summarised in Table 2.11; a full explanation of the code used is given in Appendix E.

Table 2.11: Type A uncertainty results for F_{RR} at 15 km/h, 20 kg load, following the GUM method.

Quantity	Description	Value
N	Number of trials	10
$\bar{Y}_{\text{RMS}}$	Mean of RMS values	12.879 N
$\sigma_{Y_{\text{RMS}}}$	Standard deviation of RMS values	0.0754 N
u_A	Standard deviation of the mean	0.0238 N

Type B Instrument incertainty

Type B uncertainty is evaluated for each component in the measurement chain using manufacturer specifications. Where a specification is given as a symmetric range $\pm a$, a rectangular probability distribution is assumed, giving a standard uncertainty of $u_B = \frac{a}{\sqrt{3}}$.

The rolling resistance force is given by:

$$F_{TR} = F_m + F_i + ma_x \tag{2.13}$$

The uncertainty propagation, assuming all sources are random and independent, gives:

$$u_{F_{TR}} = \sqrt{u_{F_m}^2 + u_{F_i}^2 + (m \cdot u_{a_x})^2 + (a_x \cdot u_m)^2} \tag{2.14}$$

From the calibration in Appendix B the mainloadcell has an uncertainty of 0.075N, the interface loadcell has an uncertainty of 0.19N. The ADXL335 accelerometer has a 10% sensitivity tolerance. The total mass acting on the system is 87 kg, comprising the rider, bicycle, and stabilization mechanism combined (75 kg+8 kg+4 kg). At the measured peak acceleration of 0.05 m/s^2, the accelerometer uncertainty contributes $m \cdot u_{a_x} = 87 \times 0.05 = 4.35$ N to the force uncertainty. The uncertainty of the scale used to determine the mass is not included, as its contribution is negligible relative to the accelerometer term. The full combined Type B uncertainty is therefore:

$$u_{B,F_{TR}} = \sqrt{u_{B,F_M}^2 + u_{B,F_i}^2 + (m \cdot u_{a_x})^2} = \sqrt{0.075^2 + 0.19^2 + 4.35^2} \approx 4.36\text{N} \tag{2.15}$$

Combined standard uncertainty

The Type A and Type B contributions are combined withEquation 2.7:

$$u_c = \sqrt{u_A^2 + u_B^2} = \sqrt{0.0238^2 + 4.36^2} \approx 4.36\,\text{N}. \tag{2.16}$$

The combined standard uncertainty is dominated almost entirely by the Type B contribution; the Type A repeatability term is more than two orders of magnitude smaller and has no meaningful effect on u_c.

Expanded uncertainty

Finally, the combined standard uncertainty is scaled by a coverage factor with Equation 2.8 to express the result at a defined confidence level. Using $k = 2$, corresponding to a confidence level of approximately 95 %,

$$U = k\, u_c = 2 \times 4.36 \approx 8.72\,\text{N}. \tag{2.17}$$

The rolling resistance measurement is therefore reported as $F_{\text{RR}} \pm 8.72$ N at the 95 % confidence level.

2.6.2. Spring vs. no spring

The expanded uncertainty of ± 8.72 N derived above is unacceptably large relative to the measured rolling resistance force and is dominated almost entirely by the accelerometer term. Reducing it therefore requires eliminating the $m\,a_x$ contribution, which is only present because of the accelerometer.

The accelerometer was introduced to compensate for the longitudinal movement due to a spring placed between the main loadcell and the fixed reference frame. The spring was intended to keep the main loadcell rope in tension at all times, the concern being that heavy road-induced vibrations could momentarily cause the rope to go slack and produce a corrupting zero-force reading. To test whether this was a real risk, measurements were taken without the spring. As shown in Figure 2.19, the main loadcell signal stays positive throughout the entire measurement, even under heavy vibration. The rope never goes slack, so the spring is not required and can be removed.

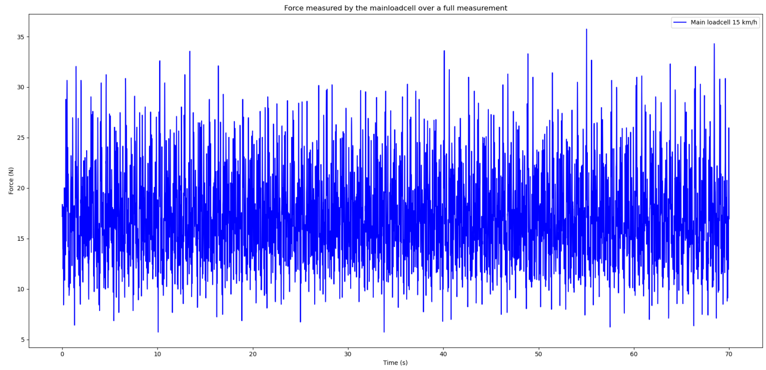

Figure 2.19: Main loadcell signal during measurement without a spring present. The signal remains positive throughout, confirming that the rope never goes slack.

With the spring removed, the measurement chain is rigid and the mass no longer undergoes significant acceleration, so the inertial correction $m\,a_x$ becomes negligible and the accelerometer can be removed as well. This has a decisive effect on the uncertainty. The dominant Type B term, the 4.35 N accelerometer contribution, disappears entirely, and the combined Type B uncertainty reduces to the loadcell contributions alone:

$$u_{B,F_{TR}} = \sqrt{u_{B,F_M}^2 + u_{B,F_i}^2} = \sqrt{0.075^2 + 0.19^2} \approx 0.20\,\text{N}, \tag{2.18}$$

a reduction of more than an order of magnitude.

To confirm that removing the accelerometer does not degrade repeatability, the Type A analysis was repeated without it under identical conditions. The results are summarised in Table 2.12. The Type A uncertainty changes only marginally, from 0.0238 N to 0.0217 N.

Table 2.12: Type A uncertainty results for F_{RR} at 15 km/h, 20 kg load, without accelerometer.

Quantity	Value
$\bar{Y}_{\text{RMS}}$	16.986 N
$\sigma_{Y_{\text{RMS}}}$	0.0686 N
u_A	0.0217 N

Combining the two sources gives a combined standard uncertainty of

$$u_c = \sqrt{u_A^2 + u_B^2} = \sqrt{0.0217^2 + 0.20^2} \approx 0.20\,\text{N}, \tag{2.19}$$

and an expanded uncertainty of $U = k\,u_c \approx 0.41$ N at the 95 % confidence level. Removing the spring, and with it the accelerometer, therefore lowers the reported uncertainty from ± 8.72 N to ± 0.41 N.

2.7. Final design

Figure 2.20 shows a CAD overview of the completed measurement apparatus without the bicycle, to clarify the position of the stabilization mechanism relative to the treadmill. The black bar represents the handlebar, which is the connection point between the bicycle and the stabilization mechanism. The 3D printed road surface is not shown in this overview.

Figure 2.20: CAD representation of the treadmill with the stabilization mechanism. The bicycle is omitted for clarity; the black bar represents the handlebar at the connection point between the bicycle and the stabilization mechanism. The 3D printed road surface is not shown.

The stabilization mechanism connects to the handlebars on both sides via the parallelogram flexures and loadcell assembly, which measure the longitudinal interface force while transmitting vertical loads directly to the mechanism frame. The two-bar linkage is fixed to the treadmill frame and constrains yaw, roll, and lateral motion of the bicycle while leaving pitch, longitudinal, and vertical motion free. The main loadcell connects the bicycle to a fixed anchor point via a rope, measuring the total horizontal resistive force. Together, the two loadcell signals are summed to obtain F_{TR} as described in section 3.3.

Figure 2.21: Photograph of the complete measurement apparatus, showing the bicycle (1), stabilization mechanism (1) and 3D printed road surface (3).

Figure 2.21 shows the complete physical measurement apparatus with the bicycle mounted, including the 3D printed road surface, all sensors, and the data acquisition system.

3

Experimental method

This chapter describes how measurements are conducted using the apparatus described in chapter 2. Section 3.1 introduces the complete assembled apparatus and its components. Section 3.2 describes the step-by-step measurement procedure followed for each trial. Section 3.3 defines how the raw sensor signals are converted to rolling resistance and powerloss. Section 3.4 describes how the resulting data is processed and analysed.

3.1. Test setup

The complete measurement apparatus is shown in Figure 3.1. It consists of a bicycle mounted on a treadmill, with a stabilization mechanism, a data acquisition system, and a safety harness. Each component is described below.

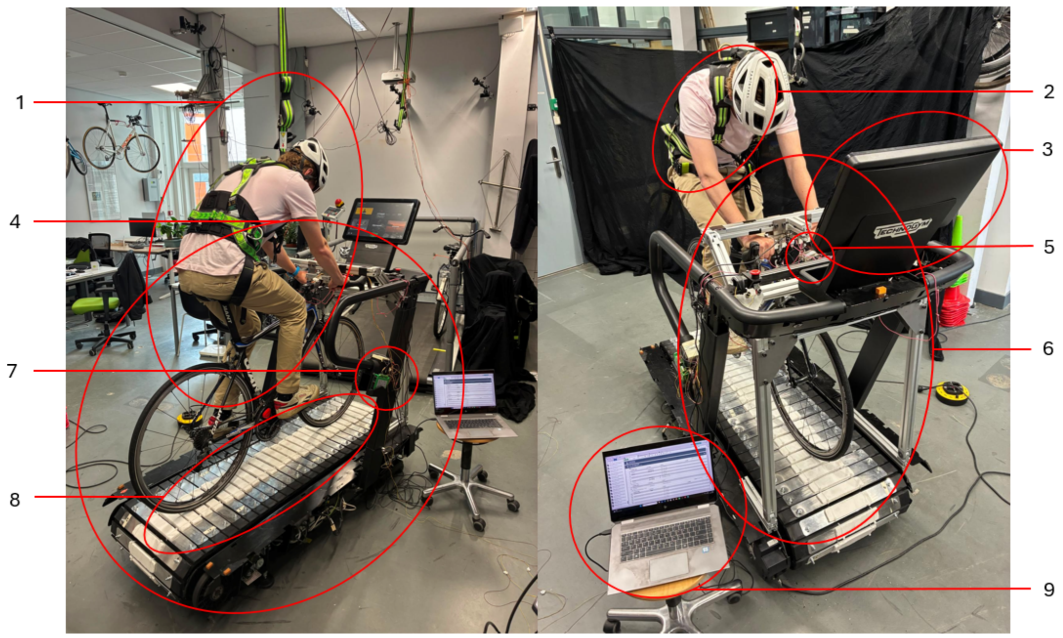

Figure 3.1: Complete measurement apparatus. (1) bicycle and rider, (2) harness, (3) treadmill touchscreen mechanism, (4) treadmill, (5) mainloadcell, (6) stabilization mechanism, (7) amplifiers, (8) 3D printed roadsurface, (9) laptop with flexlogger.

Bicycle and rider

A road bicycle is mounted on the treadmill with its tyres in contact with the road surface. A human rider sits on the bicycle in a natural riding position for the duration of each measurement. The rider does not pedal; the treadmill belt moves beneath the tyres at a controlled speed, driving them passively. The rider's body weight loads the tyres, determining the normal force at the contact patch and therefore directly influencing the rolling resistance.

The bicycle used is a Giant TCR Advanced 2012 (Giant Manufacturing Co. Ltd., Taichung, Taiwan), the same bicycle used by [5], allowing direct comparison between the two studies. The tyres are Vittoria Randonneur 700 × 28c (Vittoria S.P.A., Brembate, Italy), mounted on Shimano Dura-Ace C24 aluminium rims (622 × 15c) (Shimano Inc., Osaka, Japan).

Treadmill

A motorised treadmill provides a controlled belt surface that moves beneath the stationary bicycle tyre at a set speed. The treadmill is produced by Technogym (Technogym, Milano, Italy) and the specific type is a Skill Run (further information in Appendix C) The belt speed is set and read from the treadmill touchscreen in $\mathrm{km/h}$ and converted to $\mathrm{m/s}$ for use in the power loss calculation. The road surface tiles described in section 2.3 are bolted to the treadmill slats. So the bike will ride over the 3D printed surface and not the rubber slats from the treadmill itself.

Safety harness

The rider wears a safety harness (Kratos Safety, Heyrieux, France) connected to an overhead anchor point. The harness does not carry any load during normal operation and does not influence the measurement. It serves solely as a fall-arrest system in the event that the rider loses balance.

Stabilization mechanism

The stabilization mechanism described in section 2.4 constrains the yaw, roll, and lateral motion of the bicycle while leaving pitch, longitudinal, and vertical motion free. It connects to the handlebars via hinge joints on both sides and is fixed to the treadmill frame. The interface loadcell at the handlebar connection point measures the longitudinal force introduced by the mechanism, as described in section 2.5.

Road surface

The road surface tiles described in section 2.3 are bolted to the treadmill slats. For the measurements presented in this thesis, the klinker surface described in subsection 2.3.6 is used.

Instrumentation and data acquisition

The two Scaime ZFA load cells (Scaime, Juvigny, France) are connected to their respective Scaime CPJ signal conditioners (Scaime, Juvigny, France), which output conditioned voltage signals to the NI USB-6009 data acquisition device (National Instruments, Austin, USA). The DAQ device is connected to a laptop running FlexLogger (National instruments, Austin, USA), which records all channels to a CSV file at $100\,\mathrm{Hz}$.

3.2. Measurement procedure

Each measurement uses the following procedure. The procedure is followed identically for every trial to ensure repeatability across conditions and surfaces.

1. **Install bicycle.** Mount the bicycle on the treadmill and attach the stabilization mechanism to the handlebars. Verify that the hinge joints move freely and that the loadcell cables are connected and undamaged.
2. **Turn on powersupply and treadmill.** Power on both the treadmill and the powersupply for the amplifiers and loadcells.
3. **Tyre pressure.** Inflate both tyres to the target pressure for the trial using a calibrated pressure gauge. Verify the pressure before starting the trial.
4. **Install harness.** Fit the safety harness to the rider and connect it to the overhead anchor point. Verify that the harness is tight enough to arrest a fall but not so tight that it influences the rider's posture or loads the bicycle.
5. **Set speed.** Enter the target belt speed on the treadmill touchscreen and start the treadmill.

6. **Reach steady state.** Allow the treadmill to accelerate to the target speed. Wait until the rider is comfortable and the bike has stabilised before starting the recording. The rider is instructed to take a normal seating position, (2 hands on the handlebars, 2 feet on the pedals and in a seated position). In the remaining trials, the rider is asked to take the same position as much as possible.
7. **Record.** Start a new recording in FlexLogger. Record for $60\,\mathrm{s}$ at $100\,\mathrm{Hz}$, producing 6000 samples per channel.
8. **Activate user detection.** The treadmill is equipped with a user detection function that monitors whether a person is present on the belt at speeds above $15\,\mathrm{km/h}$. Since the rider remains stationary on the bicycle rather than running, this function must be manually satisfied. A second person applies light foot pressure to the treadmill belt every $10\,\mathrm{s}$ to maintain the detection signal. Apply gradual pressure rather than a sharp tap to avoid introducing a force drop into the loadcell signal. This is an undesirable feature of the treadmill that could not be disabled, even after consulting with the manufacturer Technogym.
9. **Stop recording.** Stop the recording in FlexLogger and stop the treadmill. Do not stop the treadmill before the logging has stopped, this will influence the measurement and slicing is necessary.
10. **Name the file.** Save the CSV file with a descriptive filename encoding the surface, speed, tyre pressure,rider and trial number, for example: `klinker_15kmh_4bar_rider_run2.csv`.
11. **Repeat.** Repeat steps 1–9 for all speed and pressure combinations in the test matrix defined in section 3.4.

3.3. Data pipeline

The raw data recorded by FlexLogger consists of a CSV file sampled at $100\,\mathrm{Hz}$, containing two voltage channels, one per loadcell. Both channels output a voltage in the range $-10\,\mathrm{V}$ to $10\,\mathrm{V}$, proportional to the applied load. The CSV file is imported in Python (3.12) and stored in a pandas (2.2.2) dataframe, after which all transformations are applied and stored as additional columns in the same dataframe. In Appendix E all the code is presented.

Each voltage channel is converted to a force using the calibration sensitivity of the respective loadcell. The interface loadcell has a sensitivity of $0.942\,\mathrm{V/kg}$ and the main loadcell has a sensitivity of $1.25\,\mathrm{V/kg}$. Both sensitivities were determined by applying known reference weights; the full calibration procedure is described in Appendix B. The conversion is applied as:

$$F = \frac{U}{S} \cdot g \tag{3.1}$$

Where F is the force in N, U is the measured voltage in V, S is the loadcell sensitivity in $\mathrm{V/kg}$, and $g = 9.81\,\mathrm{m/s^2}$. This yields the main loadcell force F_m and the interface force F_i, both in N. The total rolling resistance force is then obtained by summing the two forces:

$$F_{TR} = F_m + F_i \tag{3.2}$$

Finally, the power loss is calculated by multiplying the rolling resistance force by the treadmill belt speed:

$$P_{loss} = F_{Tr} \cdot v_{belt} \tag{3.3}$$

Where v_{belt} is the belt speed in $\mathrm{m/s}$, read from the treadmill display and converted from $\mathrm{km/h}$. The resulting P_{loss} time series for each trial is passed to the analysis described in section 3.4.

3.4. Data analysis

The goal of the data analysis is to reduce each 60-second raw force recording to a single representative value of F_{TR}, and to combine all measurements into a powerloss characterization across the full speed and pressure ranges of the treadmill and bike.

3.4.1. Rolling resistance per trial

The rolling resistance force for each trial is computed from the two calibrated load cell signals as described in section 3.3. To determine the minimum recording duration required for a stable mean, an expanding mean was computed on a representative F_{TR} time series. The expanding mean takes the cumulative mean up to each point in time, starting from the beginning of the recording, and reveals how quickly the mean stabilizes as more data is accumulated. The expanding mean converges within approximately 30 seconds. A recording duration of 60 seconds was therefore selected for all measurements, providing a safety margin of a factor of two above the stabilization time. The mean F_{TR} is then taken over the full 60-second recording. The representative value for each trial is taken as the mean of the full 60-second F_{TR} signal.

3.4.2. Powerloss per trial

The mean powerloss for each trial is calculated by multiplying the mean F_{TR} by the belt speed:

$$P_{loss} = \bar{F}_{TR} \cdot v_{belt} \tag{3.4}$$

where v_{belt} is the treadmill belt speed in m/s, read from the treadmill display and converted from km/h. This yields a single powerloss value for each combination of speed and tire pressure in the test matrix.

3.4.3. Heatmap interpolation

The 30 discrete powerloss values originate from six speed setpoints (5, 10, 15, 20, 25, 30 km/h) and five tire pressures (3.5, 4.0, 4.5, 5.0, 5.5 bar). The pressure range of 3.5 to 5.5 bar corresponds to the minimum and maximum recommended inflation pressures specified by the tyre manufacturer for the Vittoria Randonneur 700 x 28c tyre used in this study. These values are arranged on a regular grid and interpolated to produce a continuous powerloss surface. The interpolation is performed using a bivariate spline fit from the `scipy` library `RectBivariateSpline`, which fits a smooth two-dimensional spline through the measured data points. This allows the powerloss to be evaluated at any speed–pressure combination within the tested range and produces the continuous color field shown in the heatmap of Figure 4.5. The measured data points themselves are overlaid on the interpolated surface to allow direct comparison between the fitted surface and the raw values.

3.4.4. Significance assessment

To determine whether the powerloss difference between two tire pressures at a given speed is statistically meaningful, the combined measurement uncertainty from subsection 2.6.1 is propagated to a powerloss uncertainty by multiplying by the respective speed setpoint:

$$u_{P_{loss}} = u_{F_{TR}} \cdot v_{belt} \tag{3.5}$$

This uncertainty is represented as error bars in Figure 4.6 and Figure 4.7. Two tire pressures are considered significantly different at a given speed when their error bars do not overlap, following the uncertainty approach described in subsection 2.6.2. The results of this comparison are summarised in Table 4.1.

4

Results

This chapter presents the experimental results obtained from rolling resistance measurements conducted on the 3D-printed klinker road surface described in section 2.3. The measured quantity throughout is F_{TR}, the total resistive force acting on the bicycle tyre in the direction of belt travel. It is important to note that F_{TR} as defined here captures not only the classical rolling resistance due to tyre deformation, but also vibrational losses arising from road surface irregularities. The two cannot be separated with the current measurement apparatus. Results are organized into three sections: a qualitative verification of the raw sensor signals, a characterization of F_{TR} as a function of tire pressure and speed and a full powerloss characterization across tire pressure and speed.

4.1. Force Signals

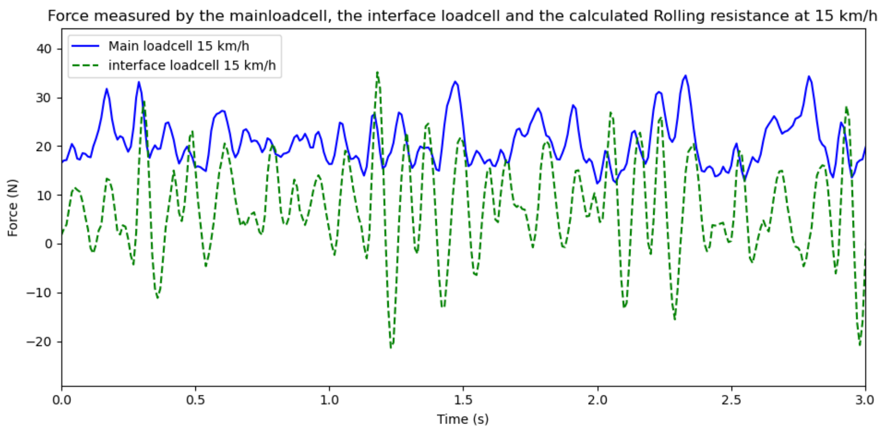

Figure 4.1: Force readout of the main loadcell and the interface loadcell at 15 km/h with a rider on the bicycle.

Figure 4.1 shows the raw force signals from both loadcells recorded at 15 km/h with a rider on the bicycle. The main loadcell signal fluctuates around 20 N and remains strictly positive throughout the measurement, confirming that the rope connecting the bicycle to the fixed reference frame never goes slack. The interface loadcell signal, by contrast, alternates between positive and negative values, indicating that the stabilization mechanism exerts both pulling and pushing forces on the bicycle during rolling. The interface loadcell signal is not centred around zero but instead oscillates about approximately 6 N. This positive offset is consistent with the geometry of the double-pendulum stabilization mechanism: since the two links are not perfectly straight in the vertical direction (like a double inverted pendulum), a net horizontal pulling force is exerted on the bicycle even in steady-state conditions.

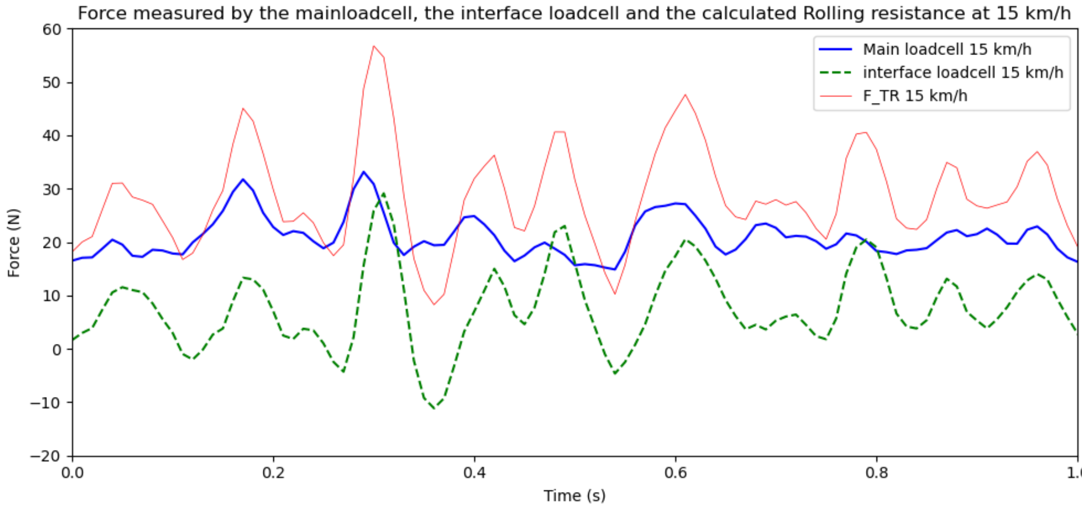

Figure 4.2: Force readout of the main loadcell, the interface loadcell, and the calculated rolling resistance F_{TR} at 15 km/h and a tire pressure of 3.5 bar.

Figure 4.2 shows the same signals as above with the calculated rolling resistance $F_{TR} = F_m + F_i$ added as a third line. The combined signal fluctuates around approximately 26 N, which is slightly above the main loadcell mean due to the 6 N offset contributed by the interface loadcell. The peak-to-peak variation in F_{TR} is larger than that of the main loadcell alone, since the force measurement of the interface loadcell is now included. These signals demonstrate that both loadcells contribute to the total measurement.

4.2. Effect of Tire Pressure and Speed on Rolling Resistance

This section characterises the mean rolling resistance force F_{TR} as a function of tire pressure and speed. Across all 30 conditions, F_{TR} ranged from 22.7 N (5.0 bar, 10 km/h) to 28.7 N (3.5 bar, 25 km/h). The same data is presented in two groupings: Figure 4.3 groups the results by tire pressure to isolate the speed dependence, and Figure 4.4 groups them by speed to isolate the pressure dependence.

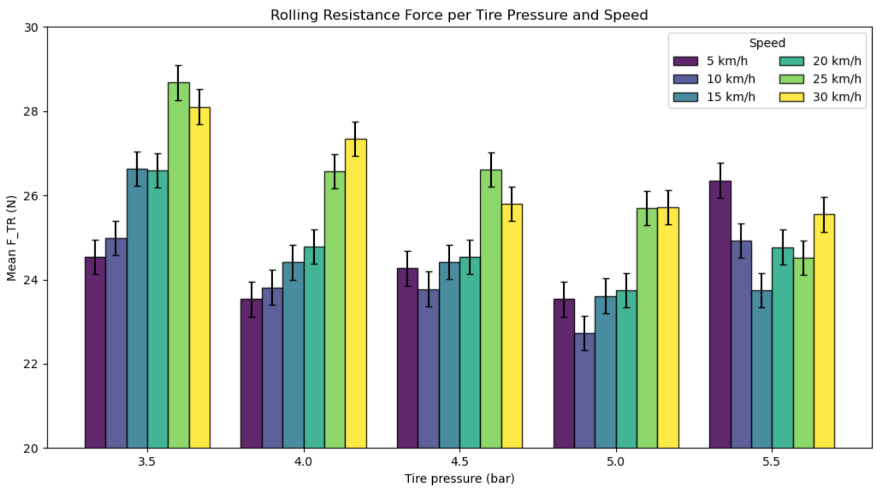

Figure 4.3: Mean rolling resistance force F_{TR} grouped by tire pressure, with each group showing the six speed setpoints (5, 10, 15, 20, 25 and 30 km/h). Error bars represent the expanded measurement uncertainty.

Speed dependence

For the four lowest pressures, F_{TR} increases monotonically with speed. The effect is strongest at the two lowest pressures: at 3.5 bar F_{TR} rises from 24.5 N at 5 km/h to 28.1 N at 30 km/h (+3.6 N, +15%), and at 4.0 bar from 23.5 N to 27.3 N (+3.8 N, +16%). At the higher pressures the linear-speed trend is not visible, with an increase of only +1.5 N (+6%) at 4.5 bar and +2.2 N (+9%) at 5.0 bar over the same interval. The 5.5 bar condition does not fit this pattern at all: F_{TR} is highest at the lowest speed (26.4 N at 5 km/h) and shows no increase with speed, ending slightly lower at 25.5 N at 30 km/h. This anomalous behaviour is discussed in chapter 5.

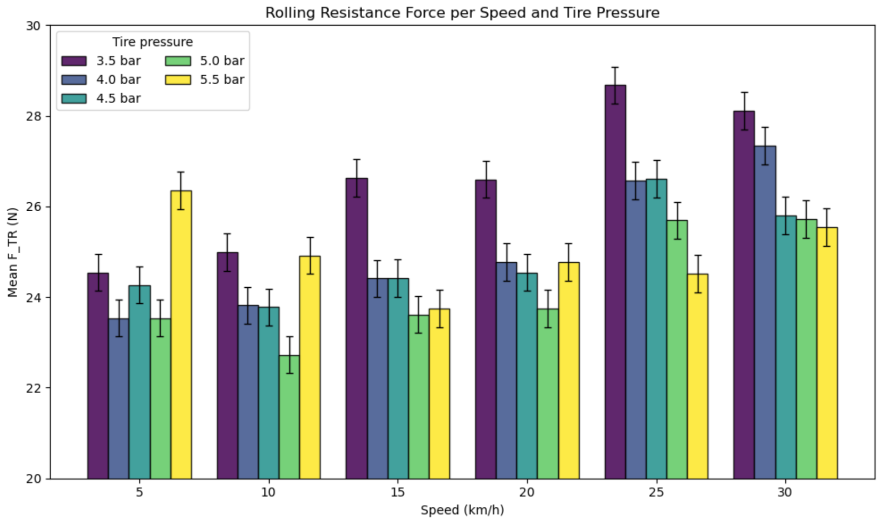

Figure 4.4: Mean rolling resistance force F_{TR} grouped by speed, with each group showing the five tire pressures (3.5, 4.0, 4.5, 5.0 and 5.5 bar). Error bars represent the expanded measurement uncertainty.

Pressure dependence

Excluding the 5.5 bar condition, a consistent pressure trend is observed at every speed of 10 km/h and above: F_{TR} is highest at 3.5 bar and lowest at 5.0 bar. This is consistent with the classical expectation that a stiffer tyre deforms less at the contact patch, reducing the rolling resistance. The magnitude of this pressure effect grows with speed: relative to the 5.0 bar value, F_{TR} at 3.5 bar is only 1.0 N (4%) higher at 5 km/h, but 2.3 N (10%) higher at 10 km/h and around 3.0 N (12–13%) higher from 15 km/h onward.

These pressure differences are well outside the measurement uncertainty. The expanded uncertainty of each individual F_{TR} value is 0.41 N, whereas the difference between the 3.5 bar and 5.0 bar conditions reaches roughly 3 N. The separation between pressures is therefore several times larger than the uncertainty of the underlying measurements, meaning the observed ordering reflects a real effect of tire pressure rather than measurement scatter.

The 5.5 bar condition again departs from the trend. Instead of continuing the reduction seen from 3.5 to 5.0 bar, it shows the highest F_{TR} of all pressures at the two lowest speeds. At 5 km/h it reaches 26.4 N, which is 2.8 N (12%) above the 5.0 bar value. At higher speeds it falls back to between the 4.5 and 5.0 bar values. As a result, 5.5 bar never produces the lowest rolling resistance at any speed, except 25 km/h.

4.3. Powerloss Characterization

The rolling resistance force alone does not fully characterize the energy cost of cycling, since the power required to overcome a given force scales directly with speed. The following figures therefore present the powerloss $P_{loss} = F_{TR} \cdot v_{belt}$, which captures the combined effect of surface resistance and riding speed.

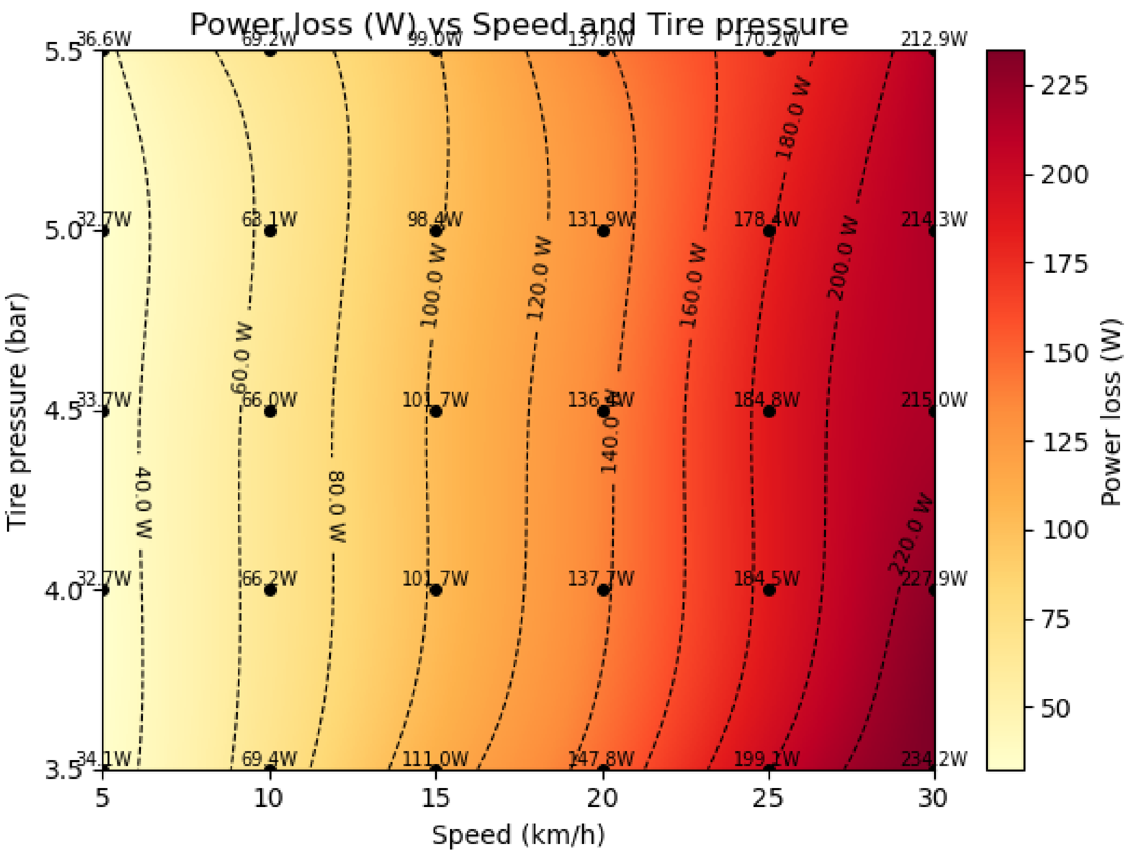

Figure 4.5: Heatmap of total powerloss as a function of speed (5–30 km/h) and tire pressure (3.5–5.5 bar). The 30 measured data points are annotated; the continuous color field is obtained by linear interpolation as described in section 3.4.

Figure 4.5 shows the powerloss as a two-dimensional heatmap over the speed (5, 10, 15, 20, 25, 30 km/h) and pressure (3.5, 4.0, 4.5, 5.0, 5.5 bar) ranges. The overall trend is dominated by speed: powerloss increases from approximately 30 W at 5 km/h to a maximum of 234.2 W at 30 km/h and 3.5 bar. At low speeds, tire pressure has a relatively modest effect on powerloss. At higher speeds the lines of constant powerloss diverge, indicating that pressure becomes a more influential parameter as speed increases. Especially at speeds above 17.5 km/h this behaviour is visable. Additionally some nonlinear behaviour is visible at the boundaries of the parameter space, particularly in the 25–30 km/h range and near 5.0–5.5 bar.

Figure 4.6 shows the powerloss as individual lines per tire pressure, with error bars representing the expanded measurement uncertainty, together with the classical rolling resistance predicted for this tyre using the C_{rr} values determined by Fernández [5] for the same bicycle, rims, and tyres. Two rolling resistance lines are shown, corresponding to the extremes of the C_{rr} range: the highest value ($C_{rr} = 0.0115$, measured at 4 bar) and the lowest value ($C_{rr} = 0.009$, measured at 5 bar). The grey band between these two lines therefore represents the range of classical rolling resistance across the tested tire pressures, while the blue region below the lowest line represents the minimum achievable rolling resistance. Both predictions are scaled to the total normal load of the present setup, which consists of an 8 kg bicycle, a 4 kg stabilization mechanism, and a 75 kg rider.

The measured powerloss (P_{TR}) increases approximately linearly with speed for all pressures, ranging from about 30 W at 5 km/h to 230 W at 30 km/h. The lines for the different pressures are closely spaced at low speed and diverge at higher speed: at 30 km/h the lowest-loss pressure (5.0 bar) and the highest-loss pressure (3.5 bar) differ by approximately 20 W, roughly 9% of the total powerloss at that speed. The error bars are small relative to the spacing between the pressure lines at most operating points, indicating that the differences between pressures are meaningful. At the lowest speeds (5–10 km/h), however, the pressure lines converge and the error bars overlap, so no meaningful difference between pressures can be claimed in that regime.

Across the whole speed range the measured powerloss lies well above the classical rolling resistance prediction; at 30 km/h the classical rolling resistance accounts for only 82 W of the approximately 230 W measured. So 64% of the total powerloss is due to vibrational losses, at 30 km/h. The interpretation of this difference is addressed in chapter 5. Zoomed-in comparisons at each speed setpoint, used to determine which individual pressure pairs differ significantly, are presented in Figure 4.7.

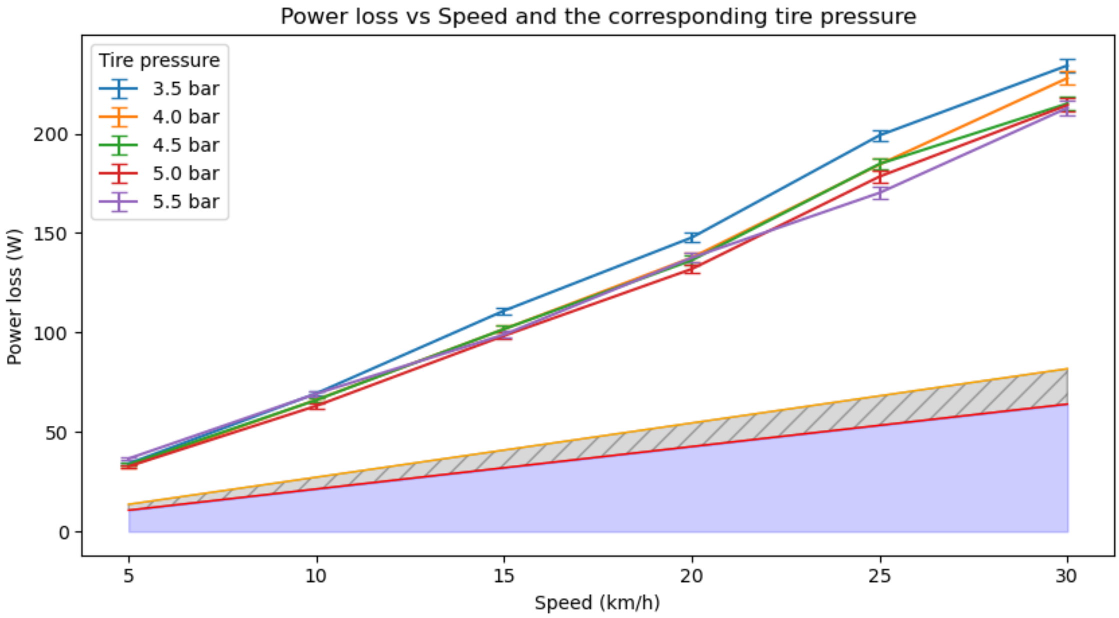

Figure 4.6: Powerloss as a function of speed for each tire pressure. The error bars represent the expanded measurement uncertainty from subsection 2.6.1, multiplied by the respective speed setpoint. The classical powerloss due to rolling resistance is also shown: the orange line corresponds to $C_{rr} = 0.009$ and the red line to $C_{rr} = 0.0115$. The grey band between them represents the range of rolling resistance powerloss across the tested tire pressures, and the blue region below the orange line represents the minimum rolling resistance powerloss.

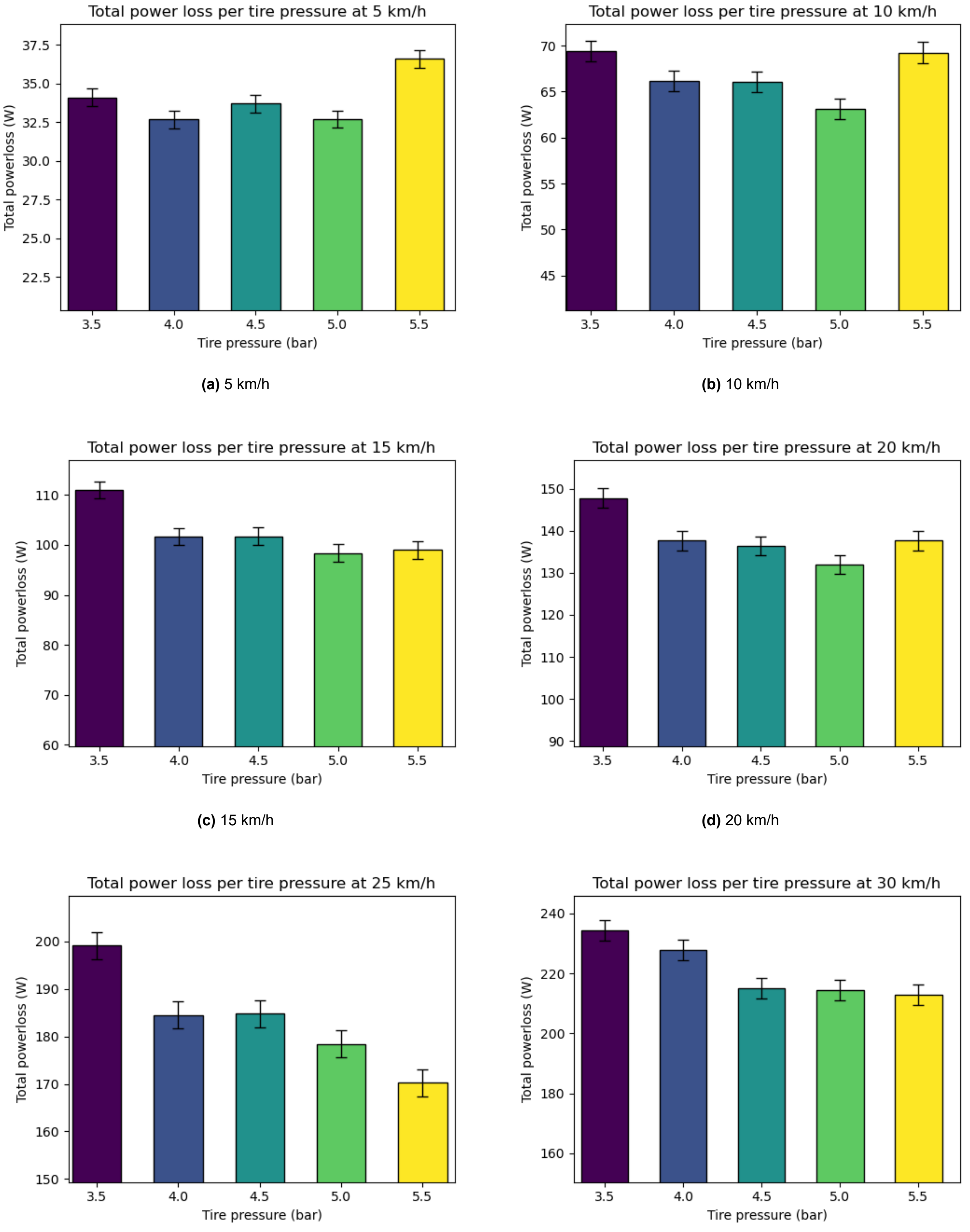

(a) 5 km/h **(b)** 10 km/h

(c) 15 km/h **(d)** 20 km/h

(e) 25 km/h **(f)** 30 km/h

Figure 4.7: Zoomed-in powerloss per speed setpoint, showing the error bars from subsection 2.6.1. Each panel shows the five tire pressures at a fixed speed. Important to note: the y-axis have different scaling on all the plots, to highlight the difference between tire pressures better.

Figure 4.7 breaks the powerloss down per speed, with one figure per speed and the y-axis rescaled in each to make the between-pressure differences visible. The figures show that the spread between pressures widens with speed: at 5 km/h all five pressures fall within a few watts of each other, whereas at 30 km/h the highest-loss pressure (3.5 bar) and the lowest exceed a 20 W gap. Across the figures, 3.5 bar produces the highest powerloss at every speed above 5 km/h, while at the highest speeds the 4.5, 5.0 and 5.5 bar bars converge.

To assess whether the observed differences in powerloss between tire pressures are meaningful, the error bars from Figure 4.7 are used to compare each pressure pair at each speed. Two pressure levels are considered distinguishable when their error bars do not overlap. The results of this comparison are summarised in Table 4.1, where ✓ indicates that the two pressures can be distinguished and × indicates that they cannot be distinguished within the expanded measurement uncertainty.

Table 4.1: Distinguishability of powerloss differences between tire pressure pairs at each speed. ✓ indicates that the two pressures can be distinguished; × indicates that they cannot be distinguished within the expanded measurement uncertainty.

Pressure pair (bar)	5 km/h	10 km/h	15 km/h	20 km/h	25 km/h	30 km/h
3.5 – 4.0	✓	✓	✓	✓	✓	×
3.5 – 4.5	×	✓	✓	✓	✓	✓
3.5 – 5.0	✓	✓	✓	✓	✓	✓
3.5 – 5.5	✓	×	✓	✓	✓	✓
4.0 – 4.5	×	×	×	×	×	✓
4.0 – 5.0	×	✓	×	✓	✓	✓
4.0 – 5.5	✓	✓	×	×	✓	✓
4.5 – 5.0	×	✓	×	×	✓	×
4.5 – 5.5	✓	✓	×	×	✓	×
5.0 – 5.5	✓	✓	×	✓	✓	×

5 Discussion

This chapter evaluates the measurement apparatus and interprets the results presented in chapter 2 and chapter 4. Section 5.1 discusses the design choices and their effect on measurement quality. section 5.2 interprets the powerloss results in the context of existing literature and examines to what extent the measured F_{TR} reflects rolling resistance versus vibrational losses. Section 5.3 summarises the main limitations of the current measurement apparatus and section 5.4 proposes directions for future research.

5.1. Design evaluation

5.1.1. Road surface

The road surface was designed to reproduce the geometry of real klinker bricks as accurately as possible, and the 3D scanning and printing pipeline achieves good geometric fidelity at the brick scale. However, the dynamic behaviour of the surface under load is influenced not only by the printed brick geometry but also by the compliance of the layers beneath it. The aluminium slats are bolted directly to the rubber treadmill slats, which are inherently compliant. Under repeated tyre loading, the rubber slats absorb part of the impact energy that would otherwise propagate into the bicycle and rider as vibration. This damping effect is expected to reduce the vibrational component of F_{TR} compared to what would be measured on a rigid foundation, since a compliant layer between the surface and the bicycle absorbs part of the impact energy that would otherwise be transmitted into the system. In future iterations of the apparatus, a more rigid underlayer, for example a steel plate, instead of rubber, would reduce this compliance and better transmit surface-induced impacts into the bicycle.

5.1.2. Stabilization mechanism

The stabilization mechanism has a total mass of approximately 13 kg, a significant portion (3.6 kg) of which is supported by the handlebars. This adds to the normal force on the front tyre beyond what a rider alone would generate, which directly increases the rolling resistance at the front contact patch. This additional load is not accounted for in the F_{TR} calculation described in section 3.3 and introduces a systematic offset in the absolute values of F_{TR} reported here. However this does not affect the relative comparison between tire pressures and speeds, since the mechanism mass is constant across all trials. It does however mean that absolute powerloss values are not directly transferable to real-world cycling conditions without correcting for this added load. A lighter mechanism, for example using thinner aluminium extrusion profiles or carbon fibre members, would reduce this effect in future iterations.

A further consequence of the current design is that yaw motion is not fully constrained. The hinge joints contain a small amount of play, which in principle allows a limited steering angle to develop if a sufficient torque is applied at the handlebars. In practice, however, this effect is negligible under normal measurement conditions: without a rider, or with a rider in a natural hands-on posture, the bicycle tracks straight without deviation. A measurable steering angle only occurs when the rider deliberately applies a large lateral force to the handlebars, which requires active effort well beyond what a normal riding posture would produce. Under the measurement conditions of this thesis, this constraint is therefore considered sufficient.

The 6 N mean offset observed in the interface loadcell signal, discussed in section 4.1, is a direct consequence of the stabilization mechanism motion. Since the stabilization mechanism is a double pendulum that does not hang perfectly vertically during measurement, it exerts a small net horizontal pulling force on the bicycle at the handlebar connection point. This force is correctly captured by the interface loadcell and included in the F_{TR} calculation, so it does not introduce an error in the total resistive measurement.

5.1.3. Sensor placement and data acquisition

The sampling rate of 100 Hz was selected based on the Nyquist criterion [23] to capture the 9–50 Hz frequency range identified by [7] as the critical range for vibrational energy dissipation in cyclists. The required sampling rate depends on the quantity of interest. For the mean rolling resistance alone, a low rate is sufficient: Fenre [10] show that a 1 Hz sampling rate already yields a precise mean estimate provided enough samples are collected, reaching a precision of ± 0.003 at only 24 samples. Resolving the vibrational content of the signal, however, requires a substantially higher rate, which is why 100 Hz was chosen here.

However, it has not been independently confirmed that 50 Hz is the true upper limit of the relevant frequency content for this apparatus and surface. Higher-frequency components, for example those arising from tyre tread impacts at 300–400 Hz [24], are not captured at 100 Hz. If these components contribute meaningfully to F_{TR}, the current apparatus would underestimate the total powerloss. A higher sampling rate would be needed to confirm that 50 Hz is indeed sufficient.

The uncertainty analysis presented in subsection 2.6.1 assumes that all measurement sources are independent. In practice, both loadcell signals are sampled by the same NI USB-6009 data acquisition device, meaning any common-mode noise or timing jitter in the DAQ affects both channels simultaneously. This introduces a correlation between the two force signals that is not accounted for in the current uncertainty propagation, and the true combined uncertainty may therefore differ from the value reported. Additionally, the pitch correction factors of 0.02% and 0.22% derived in section 2.5 are small but non-zero, and are not included in the uncertainty analysis. For the current apparatus and surface these contributions are negligible, but they would become more significant for rougher surfaces with larger pitch angles.

For rougher road surfaces that induce larger tyre displacements, the main loadcell rope may go slack during measurement, as discussed in subsection 2.6.2. In such cases a spring would need to be reintroduced into the measurement chain to maintain rope tension. However, as shown in subsection 2.6.1, including an accelerometer to account for the inertial term significantly increases the Type B uncertainty due to the 10% sensitivity tolerance of the ADXL335. A different accelerometer with better accuracy would therefore be needed to maintain measurement quality if a spring is required.

5.2. Interpretation of powerloss results

5.2.1. Comparison with vibrational loss literature

The resistive force F_{TR} results presented in section 4.2 show a near-linear dependence on speed at the lower tire pressures and a more curved, quadratic-shaped trend at the higher tire pressures. At 3.5 bar the relationship is close to a straight line, with F_{TR} increasing steadily from 24.5 N at 5 km/h to 28.1 N at 30 km/h. At 5.5 bar the trend is no longer linear: F_{TR} is 26.4 N at 5 km/h and 25.5 N at 30 km/h, curving over rather than following a straight line. So at lower pressures a linear force-speed relationship is observed, whereas at higher pressures a quadratic-shaped relationship can be seen.

Fernández [5] showed that on rough surfaces total powerloss exhibits a quadratic relationship with speed, driven by vibrational losses that grow rapidly with speed and cannot be captured by the classical $F_N C_{rr}$ formulation alone. In the present results this quadratic character is weak: it appears only at the higher pressures and produces only slight curvature. The vibrational contribution to the total loss is not small, but the speed-dependent, quadratic part of it is, which is why the force–speed relationship stays close to linear. It should also be noted that F_{TR} is multiplied by the belt speed to obtain powerloss

($P_{loss} = F_{TR}\,v$), so what little curvature is present in the force-speed relationship is largely masked once expressed as powerloss, which is why the powerloss-speed trends in Figure 4.6 appear approximately linear.

The weaker quadratic character observed here can be attributed to the difference in surface roughness between the two studies. The surfaces tested by Fernández [5] have BRI values of approximately 160, whereas the klinker surface used here has a BRI of approximately 40, comparable to a standard brick road surface. Louhghalam et al. [3] describe vibrational energy loss as being exponentially dependent on the frequency response of the vehicle, meaning that the big difference in BRI between the two studies could result in a disproportionately large reduction in vibrational powerloss. The compliance of the rubber treadmill slats beneath the printed surface, discussed in section 5.1, further damps the surface-induced impacts before they reach the bicycle, compounding this effect. This does not mean the vibrational contribution is negligible in absolute terms. As shown in Figure 4.6, at 30 km/h the classical rolling resistance predicted from the C_{rr} values of Fernández [5] accounts for only about 82 W of the roughly 230 W measured, so 64% of the total powerloss is not explained by classical rolling resistance alone. The vibrational losses are therefore large in magnitude; what the near-linear force–speed trend indicates is that their quadratic, speed-growing component is weak on this relatively smooth surface, not that the losses themselves are small.

The absolute powerloss measured here can be compared with Fernández [5], who used the same bicycle, rims, and tyres on a coast down test. Fernández reported powerlosses up to approximately 350 W, against roughly 230 W measured here at the highest speed. The lower value in the present study is consistent with two differences between the setups: the rider mass here was lower and the klinker surface used here is considerably smoother (BRI ≈ 40 versus≈ 160), producing a smaller vibrational contribution. The measured powerloss therefore falls below Fernández's values by an amount consistent with these differences, which supports the plausibility of the present results.

5.2.2. Effect of tire pressure

Classical rolling resistance predicts that powerloss falls monotonically with increasing tire pressure, since a stiffer tyre deforms less at the contact patch. A well-behaved measurement should therefore rank the five pressures in the same order at every speed. Figure 4.7 shows that this expected ordering does not hold consistently. The clearest example is the 5.5 bar condition, which produces the highest powerloss of all five pressures at 5 km/h but the lowest at 25 km/h; a single pressure cannot be simultaneously the worst and the best if tire pressure were the only factor acting. At intermediate speeds the ranking is similarly inconsistent: pressures that are clearly separated at one speed overlap at another, and in some sub figures an intermediate pressure such as 4.5 bar separates from both its neighbours while those neighbours do not separate from each other. The method therefore does not reproduce the monotonic pressure ordering that classical rolling resistance would predict.

A plausible explanation lies in rider posture variability between trials. Lépine et al. [6] demonstrated that rider posture has a large influence on the transmission of road-induced vibrations to the cyclist, with different postures producing substantially different frequency response functions between the road surface and the rider's body. Louhghalam et al. [3] show that vibrational energy loss is exponentially dependent on this frequency response, meaning that even small changes in posture could produce measurable changes in F_{TR}. The rider in this study was not a professional cyclist and acknowledged that his posture was not strictly constant between trials. Since the posture varies independently of the tire pressure being tested, it could introduce trial-to-trial variability in F_{TR} that obscures the true pressure effect and produces the irregular significance patterns observed in Table 4.1. This further motivates the use of an instrumented dummy in future measurements, which would eliminate posture variability entirely and allow the true effect of tire pressure to be isolated.

5.3. Limitations

Several limitations of the current study should be acknowledged. First, only a single road surface was tested. Although the apparatus was designed to be modular and supports multiple distinct surface configurations from the 6 scanned bricks, all measurements in this thesis were conducted in the same orientation. The effect of surface type and orientation on rolling resistance therefore remains uncharacterised.

Second, the use of a human rider introduces variability that cannot be fully controlled. As discussed in section 5.2, posture variability between trials likely contributes to the irregular significance patterns observed in Table 4.1. Despite following a consistent measurement procedure, the rider's posture was not instrumented or objectively verified between trials.

Third, although vibrational losses form a large part of the measured powerloss (about 64% of the total at 30 km/h, see subsection 5.2.1), the current surface does not excite the strong, speed-growing vibrational behaviour that was expected, in which powerloss would rise quadratically with speed. The BRI of approximately 40 is low compared with the rougher surfaces (BRI ≈ 160) on which Fernández [5] observed a clearly quadratic powerloss-speed relationship, and the compliance of the rubber treadmill slats further damps the surface-induced impacts before they reach the bicycle. As a result, the vibrational component grows only weakly quadratic with speed on this surface. This is however not a limitation of the measurement apparatus, but only the roadsurface assembly.

Fourth, two quantities in the measurement chain are taken as true value without independent verification: the treadmill belt speed and the tire pressure. The treadmill speed is read from the display and assumed to equal the actual belt speed. The treadmill uses an internal PID controller to maintain the set speed, but belt slip or controller error could introduce a systematic deviation. Since powerloss scales directly with belt speed, a speed error of even a few percent would directly affect all powerloss values. A speed sensor was integrated to verify the belt speed independently, but it could not be positioned to maintain reliable contact with the moving surface and produced an inconsistent readout, so it was not used in the final measurements. Similarly, the tire pressure is set using a calibrated pressure gauge, but the actual accuracy of this unknown. Both of these sources of systematic errors are small in practice but should be acknowledged as unverified assumptions.

Finally, the absolute powerloss values reported here are not directly transferable to real-world cycling conditions, due to the additional normal force (4 kg) introduced by the 13 kg stabilization mechanism.

Despite these limitations, the apparatus performs well against its core objectives. It measures the resistive force with an expanded uncertainty of $\pm 0.41\ N$ at the 95% confidence level. Since powerloss is obtained as $P_{loss} = F_{TR}v$, this force uncertainty translates to a powerloss uncertainty of $u_P = u_F \cdot v$, giving at most $\pm 3.4\ W$ at the highest tested speed of 30 km/h and less at lower speeds. This is small enough to resolve differences in powerloss between tire pressures at most operating points. The modular road surface supports multiple distinct surface configurations, and the stabilization mechanism holds the bicycle stable while still allowing it to move freely in the pitch, longitudinal, and vertical directions required for the tyre to roll naturally. The limitations above are therefore refinements for future iterations rather than obstacles to the core measurement, which performs as intended.

5.4. Future work

The most important direction for future work is the development of a stiffer road surface that generates sufficient vibrational excitation to produce measurable nonlinear powerloss behaviour. This requires two improvements: a more rigid underlayer beneath the printed bricks to prevent the rubber treadmill slats from damping surface-induced impacts and a rougher surface geometry with a BRI value closer to that of the surfaces tested by Fernández [5]. The possible surface configurations from the existing brick scans, as well as additional scans of rougher surface types, provide a starting point for this. Once nonlinear vibrational behaviour is visible in the powerloss data, the apparatus becomes suitable for the next research objective: quantifying how road-induced vibrations propagate through the bicycle and into the rider's body.

This second research direction, the quantification of vibration transmission to the cyclist, would ideally use an instrumented dummy in place of a human rider. A dummy eliminates posture variability between trials and allows accelerometers to be placed at fixed, reproducible locations on the body, such as the hands, seat, and feet. Combined with the force measurement already implemented in this apparatus, this would allow the full energy budget to be characterised: how much energy is dissipated at the tyre contact patch, how much propagates into the bicycle frame, and how much reaches the rider. This is directly relevant to cyclist comfort and cycling performance, particularly for riders who spend long hours on rough road surfaces.

A further improvement would be the independent verification of treadmill belt speed, for example using an optical encoder or a non-contact laser sensor measuring the belt surface directly. This would eliminate the assumption that the displayed speed equals the true belt speed and reduce a source of systematic uncertainty that currently cannot be quantified.

6
Conclusion

This thesis set out to answer the following research question:

> *What is the design of a measurement apparatus capable of measuring the powerloss experienced by a cyclist on a variable roughness road surface with quantified accuracy, and what is the effect of tire pressure and speed on powerloss for a klinker surface?*

6.1. Design of the measurement apparatus

A laboratory measurement apparatus was designed, built, and validated for measuring the powerloss experienced by a cyclist on a controlled road surface. The apparatus consists of three main components: a direct force measurement system using two Scaime ZFA loadcells, a 3D-scanned and printed klinker road surface mounted on a treadmill and a two-bar linkage stabilization mechanism connecting the bicycle to the treadmill, while allowing pitch, vertical and longitudinal motion.

The direct force measurement approach was selected over power-based alternatives because it requires no modifications to the bicycle or treadmill, minimises the measurement chain to a single loadcell per force component and is straightforward to calibrate. The stabilization mechanism constrains yaw, roll, and lateral motion while leaving pitch, longitudinal, and vertical motion free, as required for the tyre to roll naturally. A parallelogram flexure at the handlebar connection point isolates the horizontal interface force from the vertical load, allowing a single-axis loadcell to measure the longitudinal force introduced by the mechanism. The measurement uncertainty of the final apparatus is 0.20 N (Type B, instrument) and 0.0217 N (Type A, repeatability), which combine into a combined standard uncertainty of 0.20 N and an expanded uncertainty of 0.41 N at the 95% confidence level. Expressed as powerloss, this corrosponds to at most 3.4 W at 30 km/h, or about 1.5% of the total powerloss measured at that speed.

The road surface is built from six individually 3D-scanned klinker bricks, each scanned on both faces and mountable in two orientations, yielding 24 distinct klinker bricks without requiring additional scanning or manufacturing. This modularity supports the intended use of this apparatus as a platform for future research into vibration transmission.

6.2. Effect of speed and tire pressure on powerloss

Measurements were conducted across six speed setpoints (5–30 km/h) and five tire pressures (3.5–5.5 bar) on the klinker surface. The following conclusions can be drawn regarding the effect of speed and tire pressure on powerloss. Speed is the dominant factor. Powerloss increases from approximately 30 W at 5 km/h to around 230 W at 30 km/h, rising approximately linearly across the full speed range. Much of this loss is vibrational: the measured powerloss lies well above the classical rolling resistance predicted from the C_{rr} values of Fernández [5] for the same tyre, and at 30 km/h the classical term accounts for only about 82 W, so 64% of the total powerloss is not explained by classical rolling resistance alone. The vibrational contribution is therefore large in magnitude, but its speed-growing, quadratic component remains weak on this surface, consistent with the low BRI of approximately 40 and the damping of the compliant treadmill slats. The clearer quadratic speed dependence Fernández [5] observed on rougher surfaces (BRI ≈ 160) is not reproduced at this lower roughness.

Tire pressure has a smaller but measurable effect, and one that grows with speed. At low speeds the pressure lines converge and the differences fall within the measurement uncertainty, so no pressure can be distinguished as optimal. At higher speeds the pressures separate: at 30 km/h the difference in powerloss between the lowest-loss pressure (5.0 bar) and the highest-loss pressure (3.5 bar) is approximately 20 W, about 9% of the total powerloss at that speed. To put the 20 W difference in perspective, Atkinson et al. [27] report that professional cyclists sustain around 350 W on average during a time trial, so a 20 W saving corresponds to roughly 6% of the rider's total power output, a margin that could decide the outcome of a race. A consistent decrease with pressure would be expected if only classical rolling resistance were acting; the presence of a minimum instead reflects the competing pressure effects described in subsection 1.2.3, where rolling resistance falls with pressure while vibrational losses rise. This confirms that both mechanisms are active even on a relatively smooth surface. The pressure effect could not always be resolved consistently. The measured powerloss does not always rank the tire pressures in the same order across speeds, and in some cases two non-adjacent pressures cannot be told apart while the pressure between them differs from both. This is attributed to rider posture variability between trials. Small changes in posture alter how vibrations transmit through the bicycle and rider, which Lépine et al. [6] and Louhghalam et al. [3] show can measurably change energy dissipation even on smooth surfaces.

6.3. Outlook

The apparatus achieves its primary objective: it measures the total powerloss on a variable road roughness surface in a repeatable laboratory environment with quantified accuracy. The results show that vibrational losses already form a large part of this powerloss, around 64% of the total at 30 km/h. What the current surface does not yet produce is the strongly nonlinear, speed-growing vibrational behaviour seen on rougher surfaces [5]; its low roughness (BRI ≈ 40) and the compliance of the treadmill slats keep the quadratic component of the vibrational loss weak. Two improvements are needed before this apparatus can be used for its intended follow-up research: a stiffer underlayer beneath the road surface to prevent the rubber treadmill slats from absorbing surface-induced impacts and a rougher surface with a BRI value significantly above 40. Then the apparatus provides the foundation for quantifying vibration transmission from road surface through the bicycle to the rider's body, which is the next step toward understanding and reducing the energy and comfort costs of cycling on rough road surfaces.

References

[1] Michelin, *The tyre grip*, 2001.

[2] R. N. Jazar, *Vehicle Dynamics: Theory and Application: Third Edition*, English. Springer International Publishing, 2017, ISBN: 978-3-319-53441-1. DOI: 10.1007/978-3-319-53441-1.

[3] A. Louhghalam, M. Tootkaboni, and F.-J. Ulm, "Roughness-Induced Vehicle Energy Dissipation: Statistical Analysis and Scaling," *Journal of Engineering Mechanics*, vol. 141, May 2015. DOI: 10.1061/(ASCE)EM.1943-7889.0000944.

[4] M. M. Turner, "Cycling on rough roads: A model for resistance and vibration," *Vehicle System Dynamics*, vol. 62, no. 10, pp. 2729–2749, Oct. 2024, ISSN: 0042-3114. DOI: 10.1080/00423114.2024.2304031.

[5] E. V. Fernández, "Vibration Impact on Cycling Performance," en, M.S. thesis, 2025.

[6] J. Lépine, Y. Champoux, and J.-M. Drouet, "Road bike comfort: On the measurement of vibrations induced to cyclist," en, *Sports Engineering*, vol. 17, no. 2, pp. 113–122, Jun. 2014, ISSN: 1460-2687. DOI: 10.1007/s12283-013-0145-8.

[7] D. G. Wilson and T. Schmidt, *Bicycling Science*, en, 4th ed. Cambridge, MA, USA: MIT Press, May 2020, ISBN: 978-0-262-53840-4.

[8] G. Dell'Orto et al., "Vibration characterisation of strollers and cargo bicycles for transporting infants over different road surfaces," *Ergonomics*, vol. 0, no. 0, pp. 1–22, Apr. 2026, ISSN: 0014-0139. DOI: 10.1080/00140139.2026.2642987.

[9] R. Chung, "Estimating CdA with a power meter," en,

[10] M. D. Fenre, *Rolling Resistance Measurements on Cycleways Using an Instrumented Bicycle | Journal of Cold Regions Engineering | Vol 35, No 2*.

[11] F. Grappe, R. Candau, B. Barbier, M. D. Hoffman, A. Belli, and J.-D. Rouillon, "Influence of tyre pressure and vertical load on coefficient of rolling resistance and simulated cycling performance," *Ergonomics*, vol. 42, no. 10, pp. 1361–1371, Oct. 1999, ISSN: 0014-0139. DOI: 10.1080/001401399185009.

[12] B. J. Hill, "Measurement of Rolling Resistance Using an Eccentrically Weighted Oscillating Wheel," en-US, in *Surface Characteristics of Roadways: International Research and Technologies*, ASTM International, pp. 497–504. DOI: 10.1520/STP23384S.

[13] U. Sandberg, A. Bergiers, J. A. Ejsmont, L. Goubert, and M. Zöller, *Rolling Resistance : Measurement Methods for Studies of Road Surface Effects*, eng. 2012.

[14] I. Vogeler, R. Untermaierhofer, R. Petz, and T. Schütz, "Separation of Rolling Resistance and Drivetrain Losses at the Flat Belt Dynamometer," en, *ATZ worldwide*, vol. 122, no. 3, pp. 46–49, Mar. 2020, ISSN: 2192-9076. DOI: 10.1007/s38311-019-0179-z.

[15] A. Herbener and G. City, "A Direct Method of Measuring the Rolling Resistance of a Bicycle Tire," en, 2015.

[16] K. Dijkstra, "Impact of bicycle tire parameters on the total rolling losses," englsih, M.S. thesis, TU Delft, Delft, Jan. 2024.

[17] M. Guiggiani, *The Science of Vehicle Dynamics: Handling, Braking, and Ride of Road and Race Cars: Third Edition*, English. Springer International Publishing, 2023, ISBN: 978-3-031-06461-6. DOI: 10.1007/978-3-031-06461-6.

[18] Sram, *Total System Efficiency*.

[19] M. Sayers, T. Gillespie, and C. Queiroz, "INTERNATIONAL ROAD ROUGHNESS EXPERIMENT: A BASIS FOR ESTABLISHING A STANDARD SCALE FOR ROAD ROUGHNESS MEASUREMENTS.," English, *Transportation Research Record*, pp. 76–85, 1986, ISSN: 0361-1981.

[20] P. Múčka, “Simulated Road Profiles According to ISO 8608 in Vibration Analysis,” *Journal of Testing and Evaluation*, vol. 46, no. 1, pp. 405–418, Jan. 2018, ISSN: 0090-3973. DOI: `10.1520/JTE20160265`.

[21] K. Tomiyama, K. Takahasi, K. Tachibana, T. Akeda, and T. Hagiwara, “A Concept of Surface Roughness Index for Cycle Path: Bicycle Ride Index (BRI),” English, in *Lect. Notes Civ. Eng.*, vol. 523 LNCE, Springer Science and Business Media Deutschland GmbH, 2024, pp. 67–76, ISBN: 978-3-031-63583-0. DOI: `10.1007/978-3-031-63584-7_8`.

[22] D. Farhadi, *Lecture slides compliant mechanism week 5*, Delft.

[23] A. Papoulis and S. U. Pillai, *Probability, Random Variables, and Stochastic Processes*, en. McGraw-Hill, 2002, Google-Books-ID: YYwQAQAAIAAJ, ISBN: 978-0-07-112256-6.

[24] M. Levy and G. A. Smith, “Effectiveness of vibration damping with bicycle suspension systems,” en, *Sports Engineering*, vol. 8, no. 2, pp. 99–106, Dec. 2005, ISSN: 1460-2687. DOI: `10.1007/BF02844008`.

[25] BIPM et al., *Evaluation of measurement data — Guide to the expression of uncertainty in measurement*, tex.howpublished: Joint Committee for Guides in Metrology, JCGM 100:2008.

[26] G. Papaioannou and D. Koulocheris, *Experimental evaluation of wheel forces applied on a heavy vehicle and estimation of measurements uncertainty*. Apr. 2015.

[27] G. Atkinson, O. Peacock, A. St Clair Gibson, and R. Tucker, “Distribution of Power Output During Cycling,” en, *Sports Medicine*, vol. 37, no. 8, pp. 647–667, Aug. 2007, ISSN: 1179-2035. DOI: `10.2165/00007256-200737080-00001`.

A
Flexure Design

This appendix describes the design and mechanical validation of the flexures used to connect the Item 8 aluminium extrusion profile to the bicycle handlebar. The handlebar is represented in the CAD model as a circular cross-section, as shown in Figure A.1. The challenge was to create a rigid yet compliant interface that allows the load cell to register a measurable deflection while maintaining structural integrity under cyclic loading.

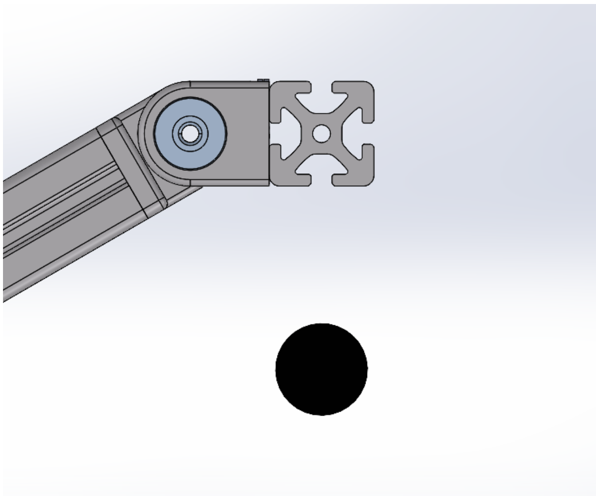

Figure A.1: Initial design situation: the aluminium extrusion profile (Item 8) to be connected to the bicycle handlebar (black circle).

Handlebar Mount

To provide a suitable mounting surface for the flexures, a dedicated handlebar mount was designed and manufactured. The mount clamps around the handlebar as shown in Figure A.2 and Figure A.4, and features through-holes to accommodate the bolts that fasten the flexures in place. The component was 3D printed in PLA with a layer height of 0.2 mm.

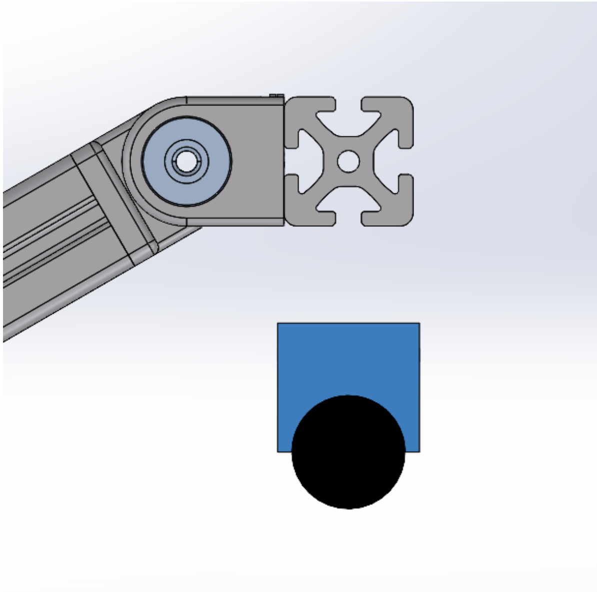

Figure A.2: Side view of the handlebar mount clamped around the handlebar.

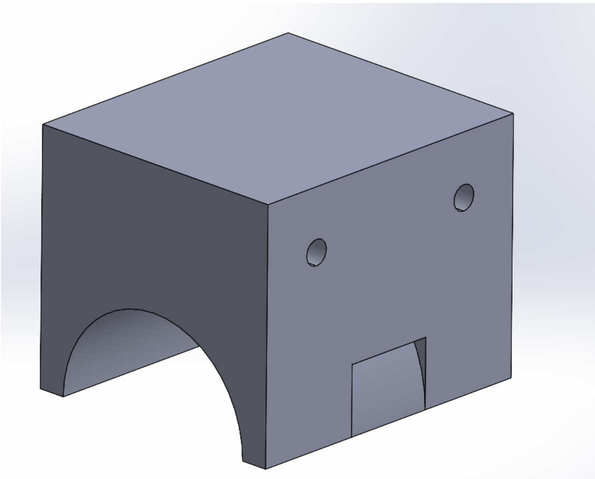

Figure A.3: Isometric view of the 3D-printed PLA handlebar mount, showing the clamping geometry and bolt through-holes. Additonally a slot is present for a hoseclamp to fixate the handlebar mount to the handlebar

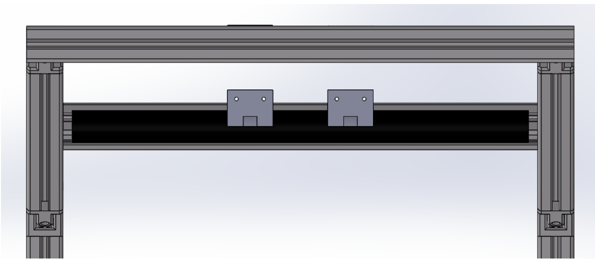

Figure A.4: Rear view of the handlebar mount as installed on the handlebar.

Two flexure assemblies are employed in total, one mounted on each side of the handlebar (left and right), to ensure a easier mounting of the bike to the stabilization mechanism.

Support Plate

To provide the flexures with a flat and well-defined mounting surface on the aluminium extrusion profile, laser-cut steel support plates were manufactured. These plates bridge the T-slot geometry of the extrusion profile and present a flat surface for the flexure attachment, as shown in Figure A.5.

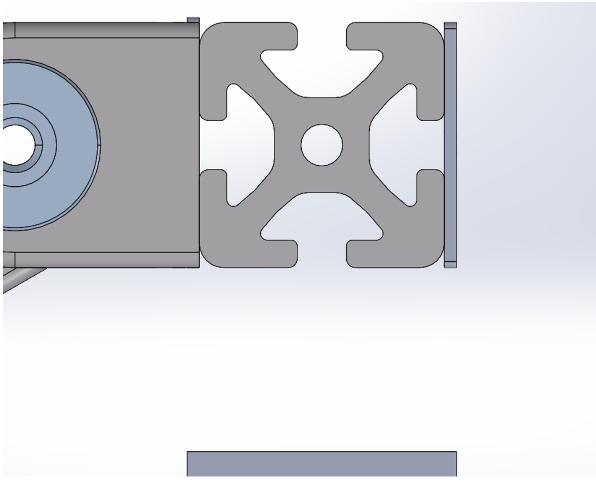

Figure A.5: Side view of the laser-cut steel support plate mounted on the aluminium extrusion profile.

Assembly

With the handlebar mounts and support plates in place, the flexures were installed to bridge the aluminium extrusion profile and the handlebars. Figure A.6 shows all four flexures installed. To prevent unintended deformation, each flexure is clamped on both sides of the aluminium extrusion profile, as visible in Figure A.7.

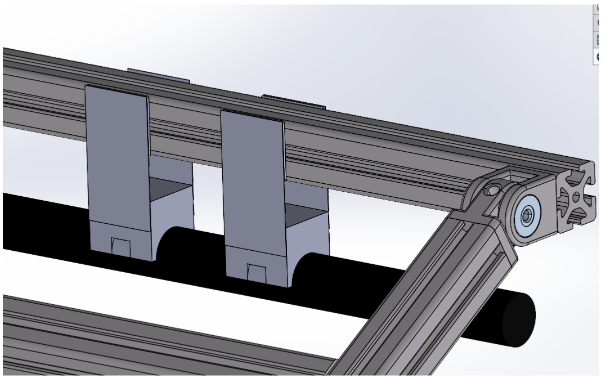

Figure A.6: All four flexures installed, connecting the aluminium extrusion profile to the handlebars.

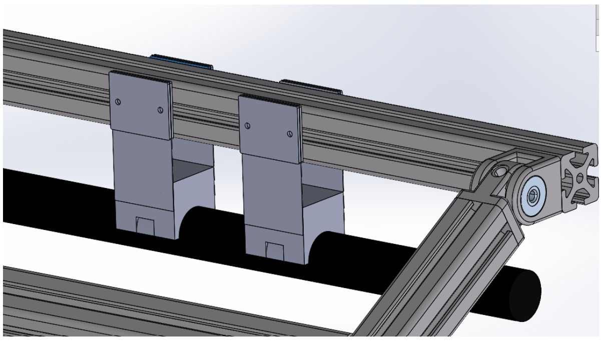

Figure A.7: Complete flexure assembly showing the handlebar mounts, flexures, and support plates. Flexures are clamped on both sides of the extrusion profile to constrain longitudinal deformation.

Finite Element Analysis

The flexures were analysed using the SolidWorks Simulation environment to verify their suitability under the expected loading conditions. The analysis assessed three design criteria: (1) infinite fatigue life, (2) yield stress margin, and (3) a minimum deflection of 1 mm under load, required for correct operation of the load cell. Buckling was additionally checked.

A simplified model was used in the FEA, as shown in Figure A.8. Although the surrounding assembly was simplified, the flexure geometry itself was kept identical to the full assembly.

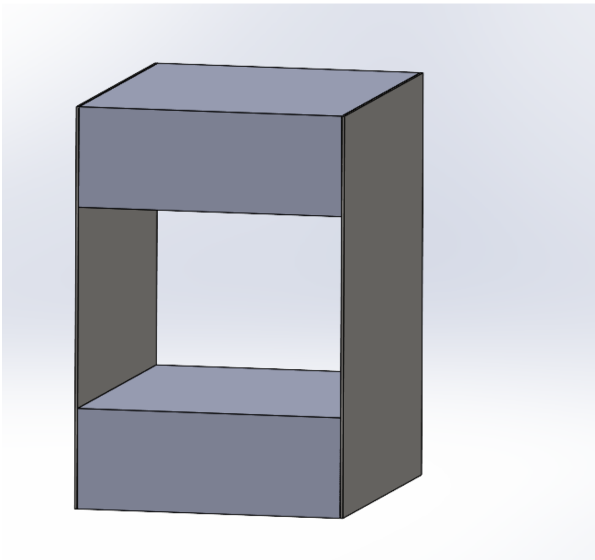

Figure A.8: Simplified FEM model of the flexure used in the SolidWorks Simulation study.

The free body diagram of the simulation is shown in Figure A.9. The handlebar mount face is modelled as a fixed support (indicated by the green arrows). A horizontal force of 60 N and a vertical force of 80 N are applied to the top face (indicated by the purple arrows), representing the expected worst-case handlebar loading during use.

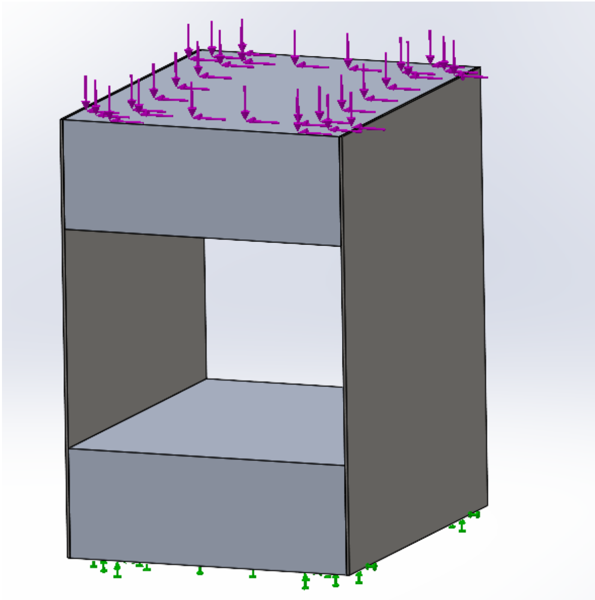

Figure A.9: Free body diagram of the FEM model: fixed supports at the base (green arrows) and applied loads of 60 N horizontal and 80 N vertical at the top face (purple arrows).

The resulting von Mises stress distribution is shown in Figure A.10. Peak stresses are concentrated in the thin flexure members, as expected. The maximum stress remains below the yield strength of the selected material.

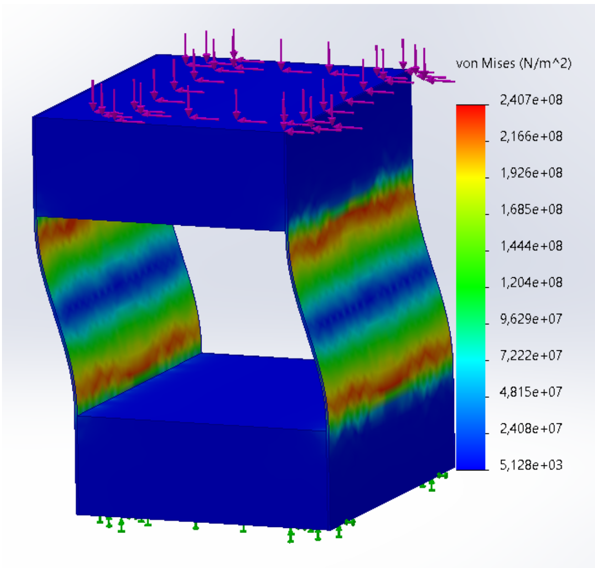

Figure A.10: Von Mises stress distribution in the flexure under static loading (units: N/m^2).

The displacement result is presented in Figure A.11. The maximum resultant displacement reaches approximately 0.96 mm, which satisfies the 1 mm deflection requirement for the load cell.

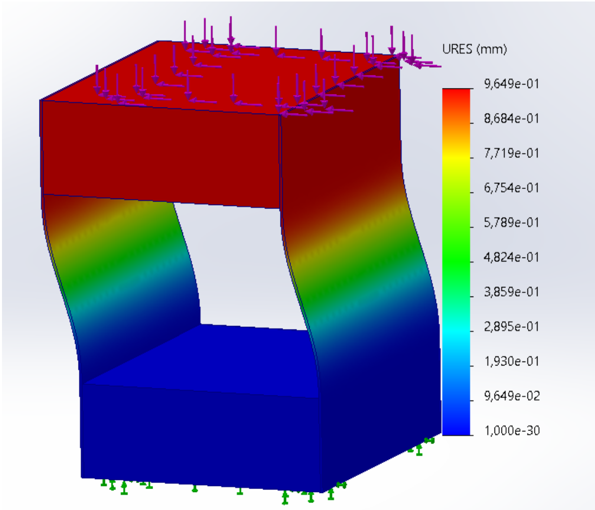

Figure A.11: Resultant displacement of the flexure under static loading (URES, units: mm). Maximum displacement is approximately 0.96 mm.

The fatigue life analysis is shown in Figure A.12. The flexure material is DIN 1.4310 spring steel, which has a fatigue endurance limit of 300 MPa due to its specific cold-rolling process. However, the SolidWorks educational licence does not include this material variant and instead applies a conservative endurance limit of 250 MPa. As a consequence, the simulation predicts fatigue failure in the thin flexure members. It should be noted that this result is a known artefact of the software's material library limitation; with the correct 300 MPa endurance limit, the design is expected to achieve infinite fatigue life under the applied loading conditions.

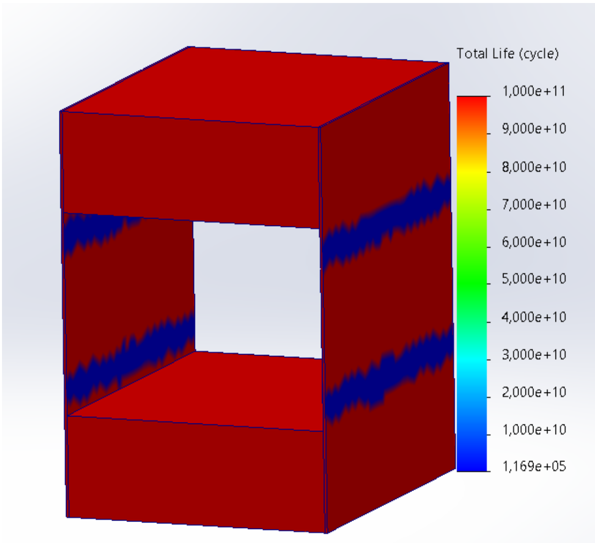

Figure A.12: Fatigue life distribution (total life in cycles). Low-life regions (blue) correspond to the thin flexure members and are attributed to the conservative 250 MPa endurance limit applied by the SolidWorks educational material library, rather than the correct value of 300 MPa for DIN 1.4310.

B

Load Cell Calibration

Two load cells were calibrated as part of this procedure: the interface load cell including its flexure mechanism, and the main load cell.

B.1. Calibration Setup

To calibrate the interface load cell, the flexure mechanism was clamped to a workbench. A metal tube was mounted to it to mimic the handlebars of the bicycle. A string was then attached to this tube, routed over a pulley, and connected to a hanging weight. This arrangement applies a horizontal pulling force to the flexure mechanism, simulating the longitudinal force the bicycle exerts on the handlebar. The setup is illustrated in Figure B.1, and the configuration with the force applied in the opposite direction is shown in Figure B.2.

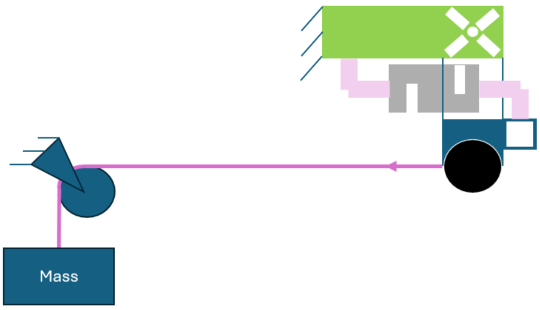

Figure B.1: Schematic of the calibration setup with force applied in the positive direction.

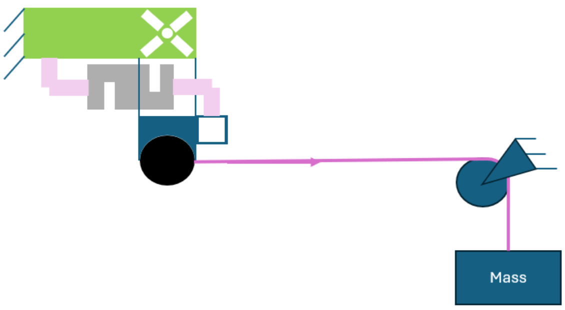

Figure B.2: Schematic of the calibration setup with force applied in the opposite direction.

A photograph of the physical setup is shown in Figure B.3.

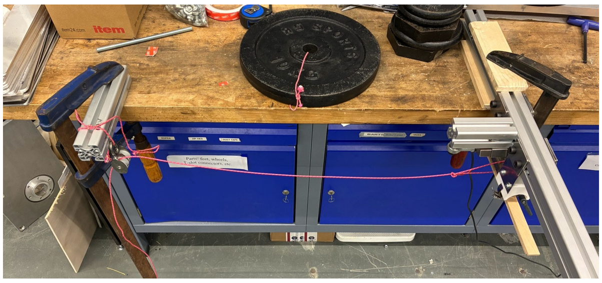

Figure B.3: Photograph of the load cell calibration setup.

B.2. Procedure

Calibration weights ranging from 0 to 7.85 kg were applied in nine steps. At each weight, the load cell output was recorded three times to assess repeatability. The procedure was then repeated with the pulley and string repositioned to the opposite side, allowing the force to be applied in the negative direction. The resulting measurements are listed in Table B.1 and Table B.2.

Table B.1: Load cell readings (V) for positive loading direction.

Appied weight (kg)	0	0.975	1.95	2.875	3.85	4.875	5.85	6.875	7.85
Measurement 1	0	0.89	1.83	2.75	3.58	4.58	5.46	6.51	7.40
Measurement 2	0	0.90	1.81	2.73	3.62	4.55	5.41	6.67	7.42
Measurement 3	0	0.91	1.82	2.74	3.62	4.53	5.47	6.55	7.45

Table B.2: Load cell readings (V) for negative loading direction.

Applied weight (kg)	0	−0.975	−1.95	−2.875	−3.85	−4.875	−5.85	−6.875	−7.85
Measurement 1	0	−0.85	−1.82	−2.71	−3.56	−4.58	−5.60	−6.68	−7.68
Measurement 2	0	−0.83	−1.82	−2.68	−3.58	−4.60	−5.58	−6.67	−7.71
Measurement 3	0	−0.88	−1.81	−2.71	−3.61	−4.57	−5.70	−6.73	−7.75

B.3. Results

A linear regression was performed on all 54 data points across both loading directions. The resulting calibration curve is shown in Figure B.4. The regression gives a sensitivity of 0.942 V/kg and a coefficient of determination of $R^2 = 0.9963$, indicating an excellent linear fit across the full measurement range.

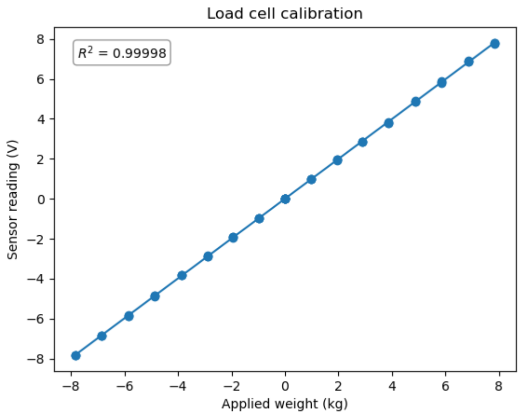

Figure B.5: Linear regression of the mainloadcell calibration measurements.

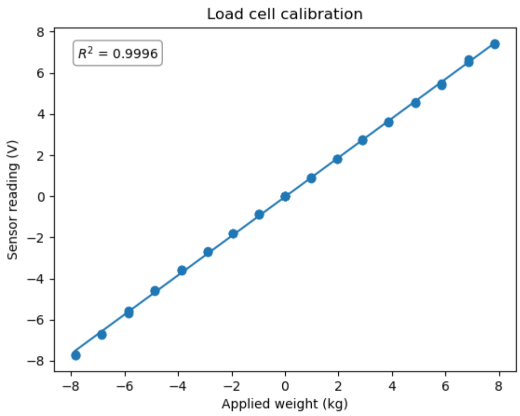

Figure B.4: Linear regression of all load cell calibration measurements, combining both positive and negative loading directions.

The strong linearity confirmed by the fit is consistent with the expected behaviour of the flexure mechanism operating within its elastic region. The calibration factor of 0.942 V/kg is therefore used to convert raw load cell output to force throughout this thesis.

The main loadcell was calibrated using the same method, and gave the following results:

C Datasheets

C.1. Scaime ZFA loadcell

The datasheet of the Scaime ZFA 0-25kg loadcell used for the force measurements is provided below.

Fiche Technique
Data Sheet

Capteurs de Pesage - Traction/compression
Load cell - Tension/compression

ZFA

25 kg ... 5 t

- Construction en acier nickelé
- Pour application de pesage et force en traction, compression ou traction/compression
- Protection IP65

- *Nickel plated steel construction*
- *Dedicated to tension, compression or tension/compression weighing or force applications*
- *Protection level IP65*

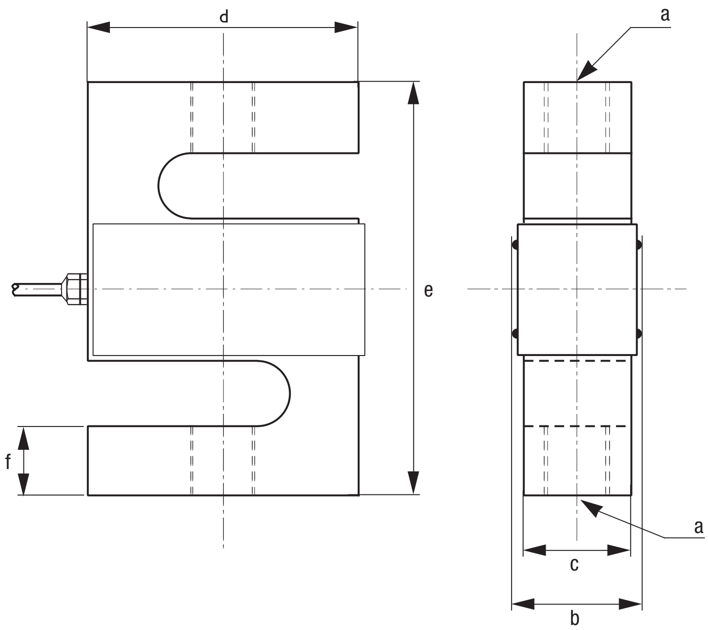

Modèle - *Model*		a	b	c	d	e	f	Poids Net - *Net Weight* [g]
25, 50	kg	M8 x 1.25	19.7	13	51	64	10.5	350
100, 200, 500	kg	M12 x 1.75	25.6	19	51	76	13.5	600
1	t	M12 x 1.75	-	25.4	54	76	13.5	750
2.5, 5	t	M18 x 1.50	-	25.4	76	108	21	1 500

Toutes dimensions en mm. Dimensions et spécifications non contractuelles. Dessins techniques disponibles sur demande.
All dimensions in mm. Dimensions and specifications do not constitute any liability whatsoever. Technical drawings are available on request.

Câblage Traction - *Tension Wiring*			
+ alim.	+ signal	- signal	- alim.
+ excit.	*+ signal*	*- signal*	*- excit.*
rouge	vert	blanc	noir
red	*green*	*whtie*	*black*

Câblage Compression - *Compression Wiring*			
+ alim.	+ signal	- signal	- alim.
+ excit.	*+ signal*	*- signal*	*- excit.*
rouge	blanc	vert	noir
red	*whit*	*green*	*black*

ZFA

25 kg ... 5 t

Caractéristiques - *Specifications*

MÉTROLOGIQUES	*METROLOGICAL*		
Capacité nominale (Cn)	*Rated capacity (Cn)*	25, 50, 100, 200, 500, 1 t, 2.5 t, 5 t	kg
Erreur combinée	*Combined error*	±0.03	%Cn
Effet de la temp. sur le zéro	*Temperature effect on zero*	±0.002	%Cn/°C
Effet de la temp. sur la sensibilité	*Temperature effect on sensitivity*	±0.002	%Cn/°C
Fluage (30 min.)	*Creep error (30 min.)*	±0.02	%Cn
Taille de plateau maximum	*Maximum platform size*	-	mm

MÉTROLOGIE LÉGALE OIML R60	*LEGAL METROLOGY OIML R60*		
Classe de précision	*Accuracy class*	-	
Capacité maximale (E_{max})	*Maximum capacity (E_{max})*	-	kg
Nombre max. d'échelons (n_{max})	*Max. number of LC intervals (n_{max})*	-	d OIML
Échelon de vérification min. (v_{min})	*Minimum verification interval (v_{min})*	-	kg
$Z=E_{max}/(2xDR)$	*$Z=E_{max}/(2xDR)$*	-	

ÉLECTRIQUES	*ELECTRICAL*		
Plage de tension d'alimentation	*Nominal range of excitation voltage*	1 ... 15	V
Sensibilité nominale à C_n	*Rated output at C_n*	3 ±0.5 %	mV/V
Plage de zéro initial	*Zero balance*	±1	%C_n
Résistance d'entrée/sortie	*Input/output resistance*	385 ±10 / 350 ±5	Ω
Résistance d'isolement	*Insulation resistance*	> 5 000	MΩ/50V

GÉNÉRALES	*GENERAL*		
Plage de temp. compensée	*Compensated temperature range*	-10 ... +50	°C
Plage de temp. de fonctionnement	*Service temperature range*	-20 ... +60	°C
Charge limite admissible	*Safe load limit*	120	%Emax
Charge ultime avant rupture	*Ultimate overload*	150	%Emax
Couple de serrage	*Tightening torque*	-	Nm
Degré de protection	*Protection class*	IP65	EN 60529
Matière	*Material*		
Corps d'épreuve	*Measuring body*	Acier nickelé - *Nickel plated steel*	
Presse étoupe	*Cable gland*	Inox - *Stainless steel*	
Gaine de câble	*Cable sheath*	*PVC*	
Longueur du câble	*Cable length*	5	m

Options - *Options*

Accessoires - *Accessoires*

Rotules - *Rod end ball joints*

scaime

Siège Social - *Headquarter*: Technosite Altéa - 294, Rue Georges Charpak - 74100 JUVIGNY - FRANCE
SCAIME SAS - 294, RUE GEORGES CHARPAK - CS 50501 - 74105 ANNEMASSE CEDEX - FRANCE
Tél. : +33 (0)4 50 87 78 64 - Fax : +33 (0)4 50 87 78 46 - info@scaime.com - www.scaime.com
Téléchargez tous nos documents sur notre site internet - *Download all our documents on our website*

C.2. Scaime cpj amplifier

The datasheet for the amplifier used in combination with the ZFA loadcell. The sensitivity used in the amplifier can be calculated using the following equation:

$$\frac{maxloadapplied}{ratedload} * sensitivity = \frac{8kg}{25kg} * 3mV/V = 0.96 \tag{C.1}$$

The CPJ amplifier datasheet is a user login protected datasheet.

C.3. ADXL335

The datasheet of the accelerometer is added below.

Small, Low Power, 3-Axis ±3 *g* Accelerometer

ADXL335

FEATURES

3-axis sensing
Small, low profile package
4 mm × 4 mm × 1.45 mm LFCSP
Low power : 350 μA (typical)
Single-supply operation: 1.8 V to 3.6 V
10,000 *g* shock survival
Excellent temperature stability
BW adjustment with a single capacitor per axis
RoHS/WEEE lead-free compliant

APPLICATIONS

Cost sensitive, low power, motion- and tilt-sensing applications
Mobile devices
Gaming systems
Disk drive protection
Image stabilization
Sports and health devices

GENERAL DESCRIPTION

The ADXL335 is a small, thin, low power, complete 3-axis accelerometer with signal conditioned voltage outputs. The product measures acceleration with a minimum full-scale range of ±3 *g*. It can measure the static acceleration of gravity in tilt-sensing applications, as well as dynamic acceleration resulting from motion, shock, or vibration.

The user selects the bandwidth of the accelerometer using the C_X, C_Y, and C_Z capacitors at the X_{OUT}, Y_{OUT}, and Z_{OUT} pins. Bandwidths can be selected to suit the application, with a range of 0.5 Hz to 1600 Hz for the X and Y axes, and a range of 0.5 Hz to 550 Hz for the Z axis.

The ADXL335 is available in a small, low profile, 4 mm × 4 mm × 1.45 mm, 16-lead, plastic lead frame chip scale package (LFCSP_LQ).

FUNCTIONAL BLOCK DIAGRAM

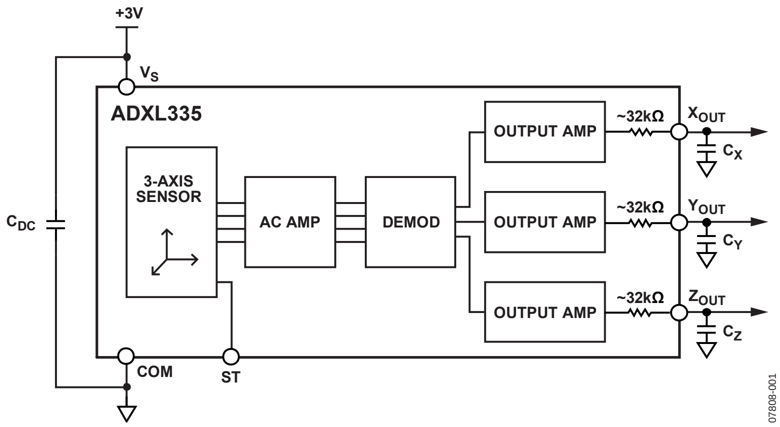

Figure 1.

Rev. B

One Technology Way, P.O. Box 9106, Norwood, MA 02062-9106, U.S.A.
Tel: 781.329.4700 www.analog.com
Fax: 781.461.3113

TABLE OF CONTENTS

REVISION HISTORY

1/10—Rev. A to Rev. B
Changes to Figure 21 ... 9

7/09—Rev. 0 to Rev. A
Changes to Figure 22 ... 9
Changes to Outline Dimensions ... 14

1/09—Revision 0: Initial Version

SPECIFICATIONS

T_A = 25°C, V_S = 3 V, C_X = C_Y = C_Z = 0.1 μF, acceleration = 0 *g*, unless otherwise noted. All minimum and maximum specifications are guaranteed. Typical specifications are not guaranteed.

Table 1.

Parameter	Conditions	Min	Typ	Max	Unit
SENSOR INPUT	Each axis				
Measurement Range		±3	±3.6		*g*
Nonlinearity	% of full scale		±0.3		%
Package Alignment Error			±1		Degrees
Interaxis Alignment Error			±0.1		Degrees
Cross-Axis Sensitivity[1]			±1		%
SENSITIVITY (RATIOMETRIC)[2]	Each axis				
Sensitivity at X_{OUT}, Y_{OUT}, Z_{OUT}	V_S = 3 V	270	300	330	mV/*g*
Sensitivity Change Due to Temperature[3]	V_S = 3 V		±0.01		%/°C
ZERO *g* BIAS LEVEL (RATIOMETRIC)					
0 *g* Voltage at X_{OUT}, Y_{OUT}	V_S = 3 V	1.35	1.5	1.65	V
0 *g* Voltage at Z_{OUT}	V_S = 3 V	1.2	1.5	1.8	V
0 *g* Offset vs. Temperature			±1		m*g*/°C
NOISE PERFORMANCE					
Noise Density X_{OUT}, Y_{OUT}			150		μ*g*/√Hz rms
Noise Density Z_{OUT}			300		μ*g*/√Hz rms
FREQUENCY RESPONSE[4]					
Bandwidth X_{OUT}, Y_{OUT}[5]	No external filter		1600		Hz
Bandwidth Z_{OUT}[5]	No external filter		550		Hz
R_{FILT} Tolerance			32 ± 15%		kΩ
Sensor Resonant Frequency			5.5		kHz
SELF-TEST[6]					
Logic Input Low			+0.6		V
Logic Input High			+2.4		V
ST Actuation Current			+60		μA
Output Change at X_{OUT}	Self-Test 0 to Self-Test 1	−150	−325	−600	mV
Output Change at Y_{OUT}	Self-Test 0 to Self-Test 1	+150	+325	+600	mV
Output Change at Z_{OUT}	Self-Test 0 to Self-Test 1	+150	+550	+1000	mV
OUTPUT AMPLIFIER					
Output Swing Low	No load		0.1		V
Output Swing High	No load		2.8		V
POWER SUPPLY					
Operating Voltage Range		1.8		3.6	V
Supply Current	V_S = 3 V		350		μA
Turn-On Time[7]	No external filter		1		ms
TEMPERATURE					
Operating Temperature Range		−40		+85	°C

[1] Defined as coupling between any two axes.
[2] Sensitivity is essentially ratiometric to V_S.
[3] Defined as the output change from ambient-to-maximum temperature or ambient-to-minimum temperature.
[4] Actual frequency response controlled by user-supplied external filter capacitors (C_X, C_Y, C_Z).
[5] Bandwidth with external capacitors = 1/(2 × π × 32 kΩ × C). For C_X, C_Y = 0.003 μF, bandwidth = 1.6 kHz. For C_Z = 0.01 μF, bandwidth = 500 Hz. For C_X, C_Y, C_Z = 10 μF, bandwidth = 0.5 Hz.
[6] Self-test response changes cubically with V_S.
[7] Turn-on time is dependent on C_X, C_Y, C_Z and is approximately 160 × C_X or C_Y or C_Z + 1 ms, where C_X, C_Y, C_Z are in microfarads (μF).

ABSOLUTE MAXIMUM RATINGS

Table 2.

Parameter	Rating
Acceleration (Any Axis, Unpowered)	10,000 *g*
Acceleration (Any Axis, Powered)	10,000 *g*
V_S	−0.3 V to +3.6 V
All Other Pins	(COM − 0.3 V) to (V_S + 0.3 V)
Output Short-Circuit Duration (Any Pin to Common)	Indefinite
Temperature Range (Powered)	−55°C to +125°C
Temperature Range (Storage)	−65°C to +150°C

Stresses above those listed under Absolute Maximum Ratings may cause permanent damage to the device. This is a stress rating only; functional operation of the device at these or any other conditions above those indicated in the operational section of this specification is not implied. Exposure to absolute maximum rating conditions for extended periods may affect device reliability.

ESD CAUTION

ESD (electrostatic discharge) sensitive device. Charged devices and circuit boards can discharge without detection. Although this product features patented or proprietary protection circuitry, damage may occur on devices subjected to high energy ESD. Therefore, proper ESD precautions should be taken to avoid performance degradation or loss of functionality.

C.4. Skillrun datasheet

This is a shortened datasheet, only the technical specifications are listed in this datasheet all the additional functions can be found online at the technogym website. In the datasheet, 3 treadmills are shown, the Unity 7000 is the treadmill used in this project. It is exactly the same as the unity 5000, however with more bio feedback functions.

TECHNICAL SPECIFICATIONS

SKILLRUN	UNITY 7000	UNITY 5000	TX 500
END-USER COMFORT AND CONVENIENCE			
Console type	Unity 3.0 19' Android open platform with HD LCD and Flat Full Glass Dual-Touch screen	Unity 3.0 19' Android open platform with HD LCD and Flat Full Glass Dual-Touch	TX 10' Android platform with HD LCD
Water bottle holder and accessory tray	Yes	Yes	Yes
Optimal View	Yes, scientifically certified display	Yes, scientifically certified display	Yes, scientifically certified display
Speed Swiftpad (Easy Access)	Yes (Homepage, Skillrun Class UI)	Yes (Homepage, Skillrun Class UI)	Yes(Skillrun Class UI)
Gradient Swiftpad (Easy Access)	Yes (Homepage,Skillrun Class UI)	Yes (Homepage, Skillrun Class UI)	Yes(Skillrun Bootcamp UI)
Fast Track Controls	Yes	Yes	Yes
Runner Detection System	Yes	Yes	Yes
Ergonomic dashboard	Yes	Yes	Yes
User-defined language selection	Yes	Yes	Yes
Languages available	24 - UK English, US English, Italian, German, Spanish, French, Dutch, Portuguese, Japanese, Chinese, Russian, Turkish, Danish, Arabic, Korean, Norwegian, Swedish, Finnish, Israeli, Catalan, Polish, Thai, Chinese simplified, Welsh	24 - UK English, US English, Italian, German, Spanish, French, Dutch, Portuguese, Japanese, Chinese, Russian, Turkish, Danish, Arabic, Korean, Norwegian, Swedish, Finnish, Israeli, Catalan, Polish, Thai, Chinese simplified, Welsh	24 - UK English, US English, Italian, German, Spanish, French, Dutch, Portuguese, Japanese, Chinese, Russian, Turkish, Danish, Arabic, Korean, Norwegian, Swedish, Finnish, Israeli, Catalan, Polish, Thai, Chinese simplified, Welsh
TECHNICAL SPECIFICATIONS AND PERFORMANCE			
Running surface type	Slat Belt technology	Slat Belt technology	Slat Belt technology
Running surface size	173 x 55 cm (68 x 22 in)	173 x 55 cm (68 x 22 in)	173 x 55 cm (68 x 22 in)
Max user weight	220 Kg / 485 lbs	220 Kg / 485 lbs	220 Kg / 485 lbs
Footrest width	14 cm (5.5 in)	14 cm (5.5 in)	14 cm (5.5 in)
Speed range (at any main supply)	0.2-30 km/h (0.1-18.6 mph)	0.2-30 km/h (0.1-18.6 mph)	0.2-30 km/h (0.1-18.6 mph)
Gradient range	-3% / +25%	-3% / +25%	-3% / +25%
Multidrive Technology	Run + Resistance	Run + Resistance	Run + Resistance
Ergonomic Sled Handlebars	Yes	Yes	Yes
Maximum Sled load	160 kg / 350 lbs	160 kg / 350 lbs	160 kg / 350 lbs
Parachute Training Kit	Included	Optional	Optional
Parachute sizes	From XS to 2XL	From XS to 2XL	From XS to 2XL
Motor PFC	Yes	Yes	Yes
Maximum resistance	1700 watts @ 10.0 km/h (6.25 mph) - [Max. Resistance increases with speed]	1700 watts @ 10.0 km/h (6.25 mph) - [Max. Resistance increases with speed]	1700 watts @ 10.0 km/h (6.25 mph) - [Max. Resistance increases with speed]
HR MONITORING			
Heart rate monitoring	Compatible with ANT+ and Bluetooth® low energy technology transmitters (chest belts)*	Compatible with ANT+ and Bluetooth® low energy technology transmitters (chest belts)*	Compatible with ANT+ and Bluetooth® low energy technology transmitters (chest belts)*
WORKOUT OPTIONS			
Classic workout programs	1 - Quick Start	1 - Quick Start	1 - Quick Start
Goal-Oriented workout programs	3 - Time/Calories/Distance	3 - Time/Calories/Distance	3 - Time/Calories/Distance
Heart rate-driven workout programs	3 - CPR-CHR/Training Zone/Weight Loss	3 - CPR-CHR/Training Zone/Weight Loss	3 - CPR-CHR/Training Zone/Weight Loss
Individual profile workout programs	7 - Profiles (6 preset), Create your own	7 - Profiles (6 preset), Create your own	7 - Profiles (6 preset), Create your own
On-trend workout programs	4 - Speed Shift, Hi-Low Blocks, Hills, Cross Training	4 - Speed Shift, Hi-Low Blocks, Hills, Cross Training	4 - Speed Shift, Hi-Low Blocks, Hills, Cross Training
Real-time Races	Up to 99 participants	Up to 99 participants	No
Marathon courses	Yes	Yes	No
Performance Training	Sled; Parachute; Run Against Resistance (constant resistance)	Sled; Parachute; Run Against Resistance (constant resistance)	Sled; Parachute
Goal-Oriented Routines	3 - Cardio Fit Training, Strong Legs, Speed&Agility Drills	3 - Cardio Fit Training, Strong Legs, Speed&Agility Drills	3 - Cardio Fit Training, Strong Legs, Speed&Agility Drills
Submaximal Tests	4 -Fitness Test, Single Stage, Multistage, Smart Test	4 -Fitness Test, Single Stage, Multistage, Smart Test	No
Maximal Tests	9 - Technogym Maximal Test, Custom Maximal Test, Bruce, Bruce Modified, Naughton, Balke And Ware, Astrand Modified, Costill And Fox, Technogym Maximal Power Test	9 - Technogym Maximal Test, Custom Maximal Test, Bruce, Bruce Modified, Naughton, Balke And Ware, Astrand Modified, Costill And Fox, Technogym Maximal Power Test	1 - Technogym Maximal Power Test
Military Tests (US Army)	8 - Gerkin Protocol, Air Force PRT, Navy PRT, Army PFT, Marine Corps PFT, Federal Law Enforcement PEB, IPPT, GTO	8 - Gerkin Protocol, Air Force PRT, Navy PRT, Army PFT, Marine Corps PFT, Federal Law Enforcement PEB, IPPT, GTO	No

*Transmitters not included

SKILLRUN	UNITY 7000	UNITY 5000	TX 500
BIOFEEDBACK (PATENT PENDING)			
Cadence	Yes	Yes	Yes
Step Length	Yes	Yes	Yes
Running Power	Yes	Yes	Yes
Ground Contact Time	Yes	Yes	Yes
Flight Time	Yes	Yes	Yes
Propulsion Time	Yes	Yes	Yes
Pushing Power	Yes (for Sled and Parachute)	Yes (for Sled and Parachute)	Yes (for Sled and Parachute)
Advanced Running Biofeedback	Yes	Optional	No
Advanced Power Biofeedback	Yes	Optional	No
FORMAT SPECIFIC UI			
Skillrun Class	Yes	Yes	No
Skillrun Bootcamp	Yes	Yes	Yes
STRUCTURAL SPECIFICATIONS			
Dimensions L x W x H	1850 x 870 x 1680 mm (73 x 34 x 66 in)**	1850 x 870 x 1680 mm (73 x 34 x 66 in)**	1850 x 870 x 1680 mm (73 x 34 x 66 in)**
Running surface height	32 cm (12.6 in)	32 cm (12.6 in)	32 cm (12.6 in)
Treadmill weight	223 kg (492 lbs)	223 kg (492 lbs)	223 kg (492 lbs)
ELECTRICAL SPECIFICATIONS			
Power requirement	200-240 Vac ("E" version); 90-240 Vac ("A" version); One dedicated 16A socket each machine	200-240 Vac ("E" version); 90-240 Vac ("A" version); One dedicated 16A socket each machine	200-240 Vac ("E" version); 90-240 Vac ("A" version); One dedicated 16A socket each machine
Power engine (peak)	10.0 HP (AC Brushless motor)	10.0 HP (AC Brushless motor)	10.0 HP (AC Brushless motor)
UTILITIES			
Maintenance	Slat belt maintenance NOT required for 160,000 km (100,000 miles)	Slat belt maintenance NOT required for 160,000 km (100,000 miles)	Slat belt maintenance NOT required for 160,000 km (100,000 miles)
OTHER FUNCTIONALITIES			
Quick and easy access	Yes	Yes	Yes
Engine belt automatic tensioning	Yes	Yes	Yes
Anterior wheels for easy transport	Yes	Yes	Yes
USB port	Yes	Yes	Yes
Customizable settings	Yes	Yes	Yes
Remote software update	Yes, with Asset Management	Yes, with Asset Management	Yes, with Asset Management
CERTIFICATIONS			
UL Mark	Yes	Yes	Yes
CE Mark	Yes	Yes	Yes
EAC Mark	Yes	Yes	Yes

** Length x Width x Height from workout position

ADVANCED BIOFEEDBACK KIT
PATENT PENDING

The optional Skillrun Advanced Biofeedback Kit consists of a sensor that allows the detection of specific running and power metrics for the left and right foot.

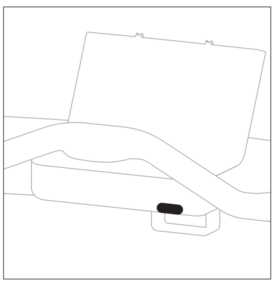

SKILLRUN PARACHUTE TRAINING KIT
PATENT PENDING A0000916

The optional Skillrun Parachute Training Kit consists of a steel frame equipped with an ergonomic adjustable belt that the users can place around their waist to perform parachute resistance training in optimized conditions.

DISPLAYS

VERSION	UNITY	TX
SCREEN AND CONTROLS		
Screen size	19" LCD - Wide 16:9	10" LCD
Android OS	Yes	Yes
Capacitive touch screen	Yes	Yes
Gesture interaction	Yes	No
TRAINING CONTENTS		
Embedded workout programs	47	16
Languages	24	24
Goal-Oriented Routines	Yes	Yes
Bootcamp UI	Yes	Yes
Sled Training	Yes	Yes
Parachute Training	Yes	Yes
Run Against Resistance Training	Yes	No
Cadence Training	Yes	Yes
3RD PARTY SOFTWARE		
Compatibility with Apple GymKit	Yes	Yes
USER ID		
Technogym key reader	Yes	Yes
Bluetooth® low energy technology	Yes	Yes
QR code	Yes	Yes
RFID (NFC) reader	Yes	Yes
Login with username and password (typing option)	Yes	Yes
Apple Watch	Yes	Yes
USER CUSTOMIZATION		
My Training Program	Yes	Yes
My Training Results	Yes	No
My Challenges	Yes	No
Favorite TV channels	Yes	No
Favorite WEB bookmarks	Yes	No
User Content Sync	Yes	No
ENTERTAINMENT OPTIONS/MULTIMEDIA		
TV	Analog Television: PAL (BG,DK,I,M,N,BG Australia), SECAM (L,L1,DK, NTSC (NTSC M). Digital Television (DVB-T HD, DVB-C HD, ATSC+QAM B mpeg2, ISDB-T (with smart card reader for Japanese market)	No
IPTV	SD; HD(MPEG-2; MPEG-4 pt 10AVC/H. 264 Standard Definition & HD - up to 720p and 1080i; Protocols: UDP multicast & unicast)	No
Radio	Yes	No
Free web browsing	Yes, customizable (Technogym App Store)	No
Games for braintraining	Yes	No
Audio-Mic Plug	Yes, Mini-jack 3,5 mm, all audio standards. MIC: CTIA/AHL standard	Yes, Mini-jack 3,5 mm, all audio standards. MIC: CTIA/AHL standard
USB Media: Audio	MP3, M4A, WAV	MP3, M4A, WAV
USB Media: Video	AVI (Video codec:XVID, MPEG4, H264 Audio codec: MP3,AC3) MKV (Video codec:MPEG4, H264 Audio codec:MP3, AAC, AC3) MP4 (Video codec: MPEG4, H264 Audio codec:MP3, AC3) Up to 720p	AVI (Video codec:XVID, MPEG4, H264 Audio codec: MP3,AC3) MKV (Video codec:MPEG4, H264 Audio codec:MP3, AAC, AC3) MP4 (Video codec: MPEG4, H264 Audio codec:MP3, AC3) Up to 720p
USB Media: Picture and documents reader	JPEG,PNG,PDF	JPEG,PNG,PDF
Smartphone, Tablet recharge	Yes*	Yes*
iPad, iPod, iPhone	Yes, via Bluetooth® connection	Yes, via Bluetooth® connection
Outdoors Virtual Training	Yes	NO

*Through USB; connection cable not provided

VERSION	UNITY	TX
CONNECTIVITY		
LAN	Yes	Yes
Wi-Fi®	Yes. Wi-Fi® IEEE 802.11b/g/n 2.4GHZ ISM Band; SECURITY: WPA/WPA2, 64,128,152-bit WEP	Yes. Wi-Fi® IEEE 802.11b/g/n 2.4GHZ ISM Band; SECURITY: WPA/WPA2, 64,128,152-bit WEP
USB	Yes	Yes
Bluetooth® low energy technology	Yes	Yes
SUPPORTED PROFESSIONAL APPS		
Communicator - Messages	Yes	No
Communicator - Club Area	Yes	No
Asset Management	Yes	Yes
Prescribe	Yes	Yes
Self	Yes	No
Challenge	Yes	No

D

Roadsurface iterations

D.1. Design of roadsurface

This appendix describes the evolution of the roadsurface used in this thesis. In total 8 iterations have been made to get a working roadsurface that was able to sustain 30 km/h and a bike and rider on top of it.

The initial idea started with some wood planks in a fishtail pattern, as can be seen in Figure D.1. The size of the wooden planks was very similiar to actual klinker bricks, this was to simulate the space constraints of actual klinker bricks.

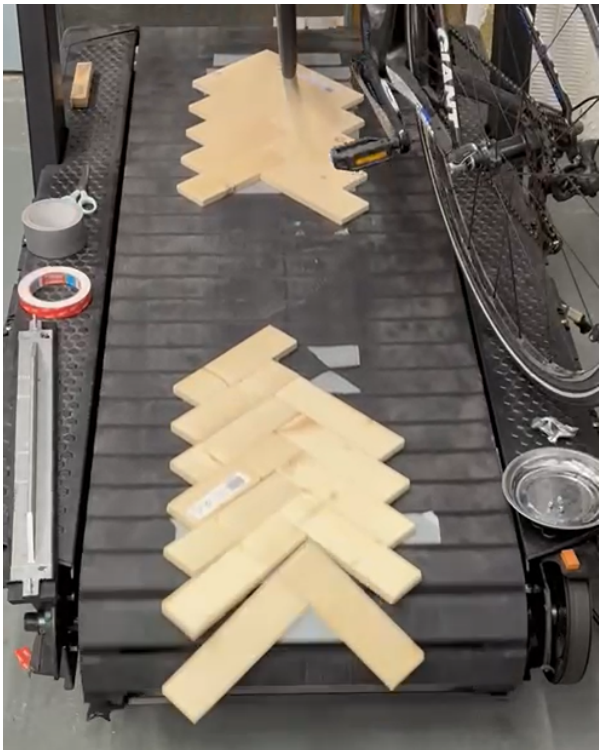

Figure D.1: Two sets of wooden planks in a fishtail pattern to simulate actual klinkers

The next step was to iterate on the wooden planks. Klinker bricks were scanned as described in chapter 2, 3D printed and glued to the alumnium slats. However after testing 2 problems started to arrise. The first problem was the 3D printed bricks were releasing from the aluminium slats. The second problem was a loud sound coming from the 3D printed bricks due to clapping noises.

The first problem was solved by using a different glue, initially a epoxy-resin glue was used. This was changed to Bison Polymax Kit. This glue is thicker and thus delivers a better contact patch between 3D print and alumnium slat. Additionally it is more flexible thus better in coping with the hard impacts.

Figure D.2: This photo was taking during the glueing process with epoxy resin glue.

This still did not adress the second problem: the load clapping sound coming from the 3D prints, if they spin around the roller. The first solution was to add padding underneath the 3D printed klinkers. This did reduce the noice, but not entirely. The main reason was that the klinkers were to close together and thus hitting each other.

Figure D.3: The klinker surface with the extra padding underneath, the photo is blurry due to it being a video originally

To solve the clashes between different 3D bricks and reduce the hard clapping noise, shorter bricks were printed. These can be seen in Figure D.4. These shorter 3D printed bricks still have the padding underneath them. Furthermore they are spaced further apart to make sure there is not clashing between bricks.

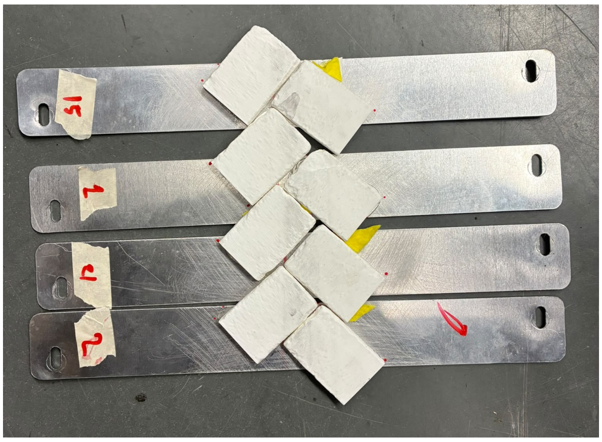

Figure D.4: Shorted klinkers (7 cm) with damping to reduce the noise.

This did however not solve the noise problem, so as a final solution. The long bricks were oriented parallel with the alumnium slats. So there would be no overlap of the 3D printed brick. This solved the noise problems, one additional tweak was necessary to make the roadsurface work correctly. Due to the high acceleration at the rollers a lot of deflection was present. To restrict this deflection, zipties have been wrapped around the 3D printed klinker, alumnium slat and the treadmill slab, as can be seen in Figure D.5. The roadsurface presented in Figure D.5 is the final roadsurface setup used in this thesis.

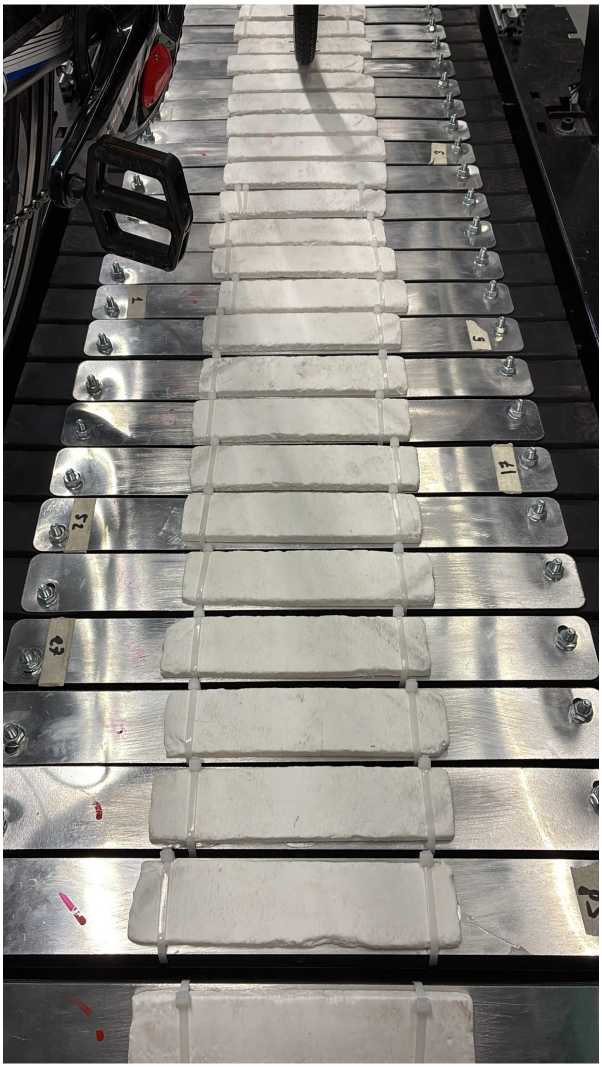

Figure D.5: The final version of the roadsurface used in this thesis.

E
Code

All the code used in this thesis is uploaded in the surf drive of this thesis, with READ.ME files.